REPORT DOCUMENTATION PAGE

Form Approved
OMB No. 0704-0188

Public reporing burden for this collection of information is estimated to average 1 hour per response, including the time for reviewing instructions, searching existing data sources, gathering and maintaining the data need ed, and completing and reviewing the collection of information. Send comments regarding this burden estimate or any other aspect of this collection of information, including suggestions for reducing this burden, to Washington Headquarters Services, Directorate for information Operations and Reports, 1215 Jefferson Davis Highway, Suite 1204, Arlington, VA 22202-4302, and to the Office of Management and Budget, Paperwork Reduction Project (0704-0188), Washington, DC 20503.

1. Agency Use Only (Leave Blank).	2. Report Date. April 2001	3. Report Type and Dates Covered. Final Report	
4. Title and Subtitle. **Workshop on Imaging of Complex Media with Acoustic and Elastic Waves**			**5. Funding Numbers.** N00014-99-1-0220
6. Author(s). W. Kuperman			Project No. Task No.
7. Performing Monitoring Agency Names(s) and Address(es). University of California, San Diego Marine Physical Laboratory Scripps Institution of Oceanography San Diego, California 92152			**8. Performing Organization Report Number.**
9. Sponsoring/Monitoring Agency Name(s) and Address(es). Office of Naval Research Ballston Centre Tower One 800 North Quincy Street Arlington, VA 22217-5660 Jeffrey Simmen, ONR 321OA			**10. Sponsoring/Monitoring Agency Report Number.**
11. Supplementary Notes.			
12a. Distribution/Availability Statement. Approved for public release; distribution is unlimited.			**12b. Distribution Code.**

13. Abstract (Maximum 200 words).

A workshop was held to introduce new developments in acoustics and signal processing in the field of ocean acoustics and tomography, laboratory ultrasonics, seismology and medical ultrasonics. The underlying theme is time reversal acoustics.

20040809 082

14. Subject Terms. capillary waves, ocean surface, internal wave interaction, remote sensing			15. Number of Pages. 10
			16. Price Code.
17. Security Classification of Report. Unclassified	18. Security Classification of This Page. Unclassified	19. Security Classification of Abstract.. Unclassified	20. Limitation of Abstract. None

NSN 7540-01-280-5500

Standard Form 298 (Rev. 2-89)
Prescribed by ANSI Std. 239-18 298-10

Workshop on Imaging of Complex Media with Acoustic and Elastic Waves

W. Kuperman

Abstract

The objective of this workshop was to cross-fertilize new developments
in acoustics and signal processing in the field of ocean acoustics and
tomography, laboratory ultrasonics, seismology and medical ultrasonics.
The workshop was held in Cargese, Corsica (France). Groups of 15
leading scientific researcheers presented lectures in each of their
respective fields.

Research Summary

The workshop combined a tutorial approach in providing a common
interdisciplinary basis with presentations and discussions of the latest
research results. Contributions (13) of each of the discussions were
compiled in a workshop proceedings entitled, "Imaging of Complex
Media with Acoustic and Seismic Waves" and submitted to Springer-
Verlag GmBH & Co., Germany for publishing.

A chapter entitled, "Ocean Acoustics, Matched Field Processing and
Phase Conjugation" by W. A. Kuperman and D. R. Jackson is included
from the book as submittal of the reporting requirements under this grant.

Ocean Acoustics, Matched Field Processing and Phase Conjugation

W. A. Kuperman
Scripps Institution of Oceanography
Marine Physical Laboratory
University of California, San Diego
La Jolla, CA 92093-0701
email: wkuperman@ucsd.edu

D. R. Jackson
Applied Physics Laboratory
College of Ocean and Fishery Sciences
University of Washington
Seattle, WA 98105-6698
email: drj@apl.washington.edu

INTRODUCTION

This chapter treats ocean acoustics and various applications of signal processing, phase conjugation and tomography to ocean acoustics. Phase conjugation is related to the standard principles of passive signal processing and to the more recent demonstrations of time reversal mirrors in the ocean. Here we will overview relevant physics of ocean acoustics, present a passive signal processing method called matched field processing and then discuss the related concept and implementation of time reversal methods in ocean acoustics.

1 Review of Ocean Acoustics

The ocean is a waveguide, bounded above by a pressure release surface and below by a visco-elastic medium. The physical oceanographic parameters, as ultimately represented by the ocean sound speed structure, make up the index of refraction of the water column waveguide. The combination of water column and bottom properties leads to a set of generic sound propagation paths descriptive of most propagation phenomena in the ocean.
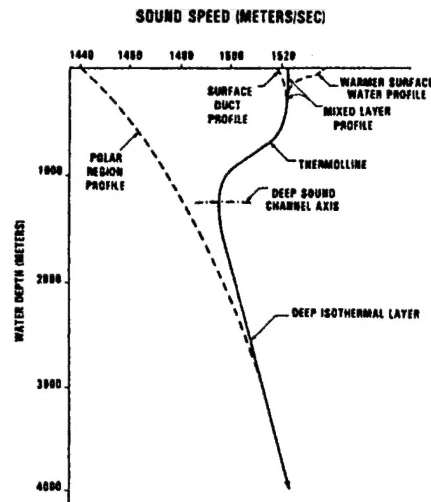
Figure 1: Generic sound speed profiles

1.1   QUALITATIVE DESCRIPTION OF OCEAN SOUND PROPAGATION

First we summarize aspects of oceanography that impact propagation paths before we go into more detail on the propagation itself. Figure 1 illustrates a typical set of sound speed profiles indicating greatest variability near the surface as a function of season and time of day. In a warmer season (or warmer part of the day), the temperature increases near the surface and hence the sound speed decreases with depth. In nonpolar regions, the oceanographic properties of the water near the surface result from mixing activity originating from the air-sea interface. This near surface mixed layer has a constant temperature (except in calm, warm surface conditions as described above). In this isothermal mixed layer, the sound speed profile can increase with depth due to the pressure gradient effect. This is the "surface duct" region.

1.1.1   Sound Propagation Paths in the Ocean

Below the mixed layer is the thermocline in which the temperature decreases with depth and the sound speed decreases with depth. Below the thermocline, the temperature is constant and the sound speed increases because of increasing pressure. Therefore, there exists a depth between the deep isothermal region and the mixed layer with a minimum in sound speed; this depth is often referred to as the axis of the deep sound channel.

However, in polar regions, the water is coldest near the surface and hence the minimum sound speed is at the ocean/air(or ice) interface as indicated in Fig. 1 In continental shelf regions (shallow water) with water depths on the order of a few hundred meters, only the upper region of the sound speed profile in Fig. 1, which is dependent on season and time of day, affects sound propagation in the water column.

Figure 2 is a contour display of the sound speed structure of the North and South Atlantic [1] with the axis of the deep sound channel indicated by the heavy dashed line. Note the geographic(and climatic) variability of the upper ocean sound speed structure and the stability of this structure in the
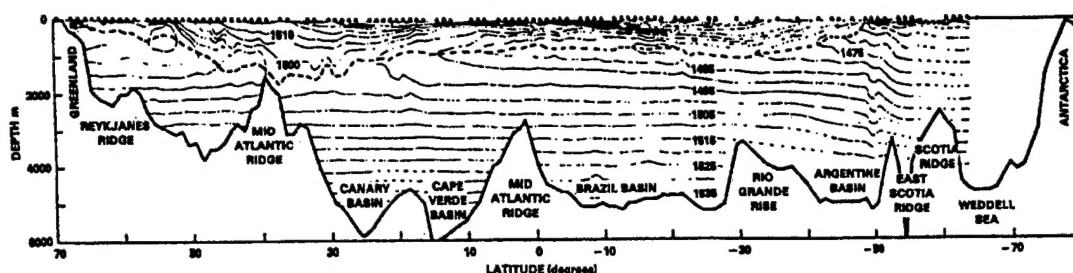
Figure 2: Sound speed contours at 5 m/s intervals taken from the North and South Atlantic along 30.50 degrees West. Dashed line indicates axis of deep sound channel (from Northrup and Colburn, 1974).

deep isothermal layer. For example, as explained above, the axis of the deep sound channel becomes shallower toward both poles, eventually going to the surface. Figure 3 is a schematic of the basic types of propagation in the ocean resulting from the sound speed profiles (indicated by the dashed lines) discussed in the last section. These sound paths can be understood from a simplified statement of Snell's Law: sound bends locally toward regions of low sound speed (or sound is "trapped" in regions of low sound speed). Paths A and B correspond to surface duct propagation where the minimum sound speed is at the ocean surface (or at the bottom of the ice cover for the Arctic case). Path C, depicted by a ray leaving a deeper source at a shallow horizontal angle propagates in the deep sound channel whose axis is at the shown sound speed minimum. This local minimum tends to become more shallow towards polar latitudes converging to the Arctic surface minimum. Hence for mid latitudes, sound in the deep channel can propagate long distances without interacting with lossy boundaries; propagation via this path has been observed over distances of thousands of kilometers. Also, from the above description of the geographical variation of the acoustic environment combined with Snell's Law, we can expect that shallow sources coupling into the water column at polar latitudes will tend to propagate more horizontally around an axis which becomes deeper toward the mid latitudes. Path D, which is at slightly steeper angles than those associated with path C, is convergence zone propagation, a spatially periodic ($\sim 35 - 65$ km) refocusing phenomenon producing zones of high intensity near the surface due to the upward refracting nature of the deep sound speed profile. Referring back to Fig. 1, there may be a depth in the deep isothermal layer at which the sound speed is the same as it is at the surface. This depth is called the "critical depth" and, in effect, is the lower limit of the deep sound channel. A "positive critical depth" specifies that the environment supports long distance propagation without bottom interaction, whereas "negative" implies that the bottom ocean boundary *is* the lower boundary of the deep sound channel. The bottom bounce path, E, which interacts with the ocean bottom is also a periodic phenomenon but with a shorter cycle distance and a shorter total propagation distance because of losses when sound is reflected from the ocean bottom. Finally, the right hand side of Fig. 3 depicts propagation in a shallow water region such as a continental shelf. Here sound is channeled in a waveguide bounded above by the ocean surface and below by the ocean bottom.

The modeling of sound propagation in the ocean is further complicated because the environment varies laterally (range dependence), and all environmental effects on sound propagation are dependent on acoustic frequency in a rather complicated way which often makes the ray type schematic of Fig.
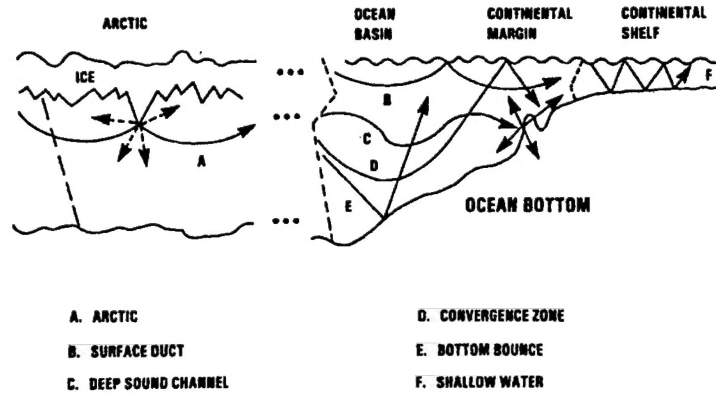
Figure 3: Schematic representation of various types of sound propagation in the ocean.

3 misleading, particularly at low frequencies. Finally, a quantitative understanding of acoustic loss mechanisms in the ocean is required for modeling sound propagation. These losses are, aside from geometric spreading: volume attenuation, bottom loss (i.e., a smooth water/bottom interface is not a perfect reflector), and surface, volume (including fish) and bottom scattering loss. Here we will only review those aspects of bottom loss which impact propagation structure.

1.1.2 Bottom Loss

Ocean bottom sediments are often modeled as fluids since the rigidity (and hence the shear speed) of the sediment is usually considerably less than that of a solid, such as rock. In the latter case, which applies to the "ocean basement" or the case where there is no sediment overlying the basement, the medium must be modeled as an elastic solid which means it supports both compressional and shear waves.

Reflectivity, the amplitude ratio of reflected and incident plane waves at an interface separating two media, is an important measure of the effect of the bottom on sound propagation. For an interface between two fluid semi-infinite halfspaces with density ρ_i and sound speed c_i, $i = 1, 2$, as shown in Fig. 4(a) (assuming a harmonic time dependence of $\exp(-i\omega t)$), the reflectivity is given by

$$\mathcal{R}(\theta) = \frac{\rho_2 k_{1z} - \rho_1 k_{2z}}{\rho_2 k_{1z} + \rho_1 k_{2z}}, \tag{1}$$

with

$$k_{iz} = (\omega/c_i)\sin\theta_i \equiv k_i \sin\theta_i \; ; \; i = 1, 2. \tag{2}$$

The incident and transmitted grazing angles are related by Snell's Law,

$$k_\perp = k_1 \cos\theta_1 = k_2 \cos\theta_2, \tag{3}$$

where the incident grazing angle θ_1 is also equal to the angle, θ_R, of the reflected plane wave. $\mathcal{R}(\theta)$ is also referred to as the *Rayleigh Reflection Coefficient* and has unit magnitude (total internal reflection) when the numerator and denominator of Eq. 1 are complex conjugates. This occurs when k_{2z} is purely
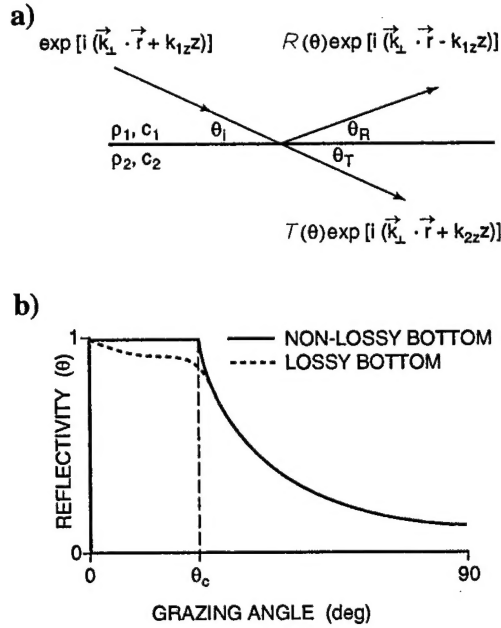
a)

b)

Figure 4: The reflection and transmission process. Grazing angles are defined relative to the horizontal.

imaginary and, using Snell's Law for determining θ_2 in terms of the incident grazing angle, we obtain the *critical grazing angle* below which there is perfect reflection,

$$\cos \theta_c = c_1/c_2, \tag{4}$$

so that a critical angle can exist only when the speed in the second medium is higher than that of the first.

Using Eq. 2, Eq. 1 can be rewritten as

$$\mathcal{R}(\theta) = \frac{\rho_2 c_2/\sin \theta_2 - \rho_1 c_1/\sin \theta_1}{\rho_2 c_2/\sin \theta_2 + \rho_1 c_1/\sin \theta_1} \equiv \frac{Z_2 - Z_1}{Z_2 + Z_1}, \tag{5}$$

where the right hand side is in the form of *impedances*, $Z_i(\theta_i) = \rho_i c_i/\sin \theta_i$, which are the ratios of the pressure to the vertical particle velocity at the interface in the ith medium. Written in this form, the reflectivity for more complicated boundaries follows in a straightforward manner [2].

In lossy media, attenuation can be included in the reflectivity formula by taking the sound speed as complex so that the wavenumbers are subsequently also complex, $k_i \rightarrow k_i + \alpha_i$.

Figure 4(b) depicts a simple bottom *loss* curve derived from the Rayleigh reflection coefficient formula where both the densities and sound speed of the second medium are larger than those in the first medium with unit reflectivity indicating perfect reflection. For loss in dB, 0 dB is perfect reflecting, 6 dB loss is an amplitude factor of one-half, 12 dB loss is one-fourth, etc. For a lossless bottom, severe loss occurs above the critical angle in the water column due to transmission into the bottom. For the lossy (more realistic) bottoms, only partial reflection occurs at all angles. With paths involving many bottom bounces (shallow water propagation), bottom losses as small as a few-tenths of a dB per bounce accumulate and become significant because the propagation path may involve many tens of bounces.
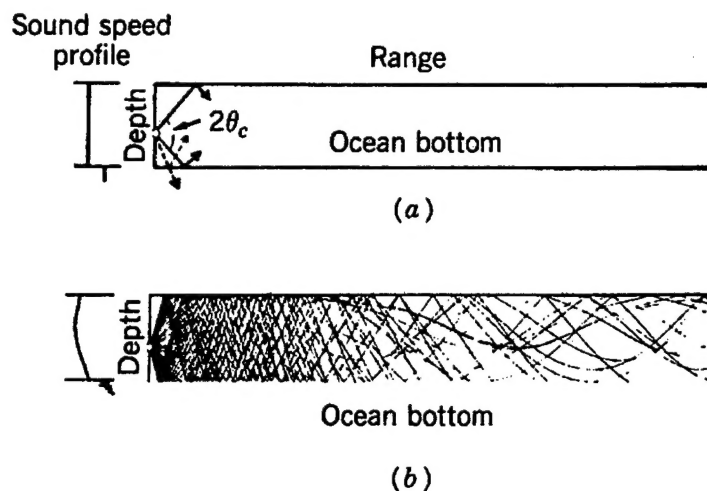
Sound speed profile

Figure 5: Ocean waveguide propagation. (a) Long distance propagation occurs within a cone of $2\theta_c$. (b) Same as (a) but with nonisovelocity water column showing refraction.

Path E in Fig. 3, the bottom bounce path, often involves paths which correspond to angles near or above the critical angle; therefore, after a few bounces, the sound level is highly attenuated. On the other hand, for shallow angles, many bounces are possible. Hence, in shallow water, path F, most of the energy that propagates is close to the horizontal and this type of propagation is most analogous to waveguide propagation. In fact, as shown in Fig. 5, there exists a small cone from which energy propagates long distances (θ_c is typically $10° - 20°$). Energy outside the cone is referred to as the near field (or continuous spectrum), which eventually escapes the waveguide. The trapped field originating from within the cone is referred to as the normal mode field (or discrete spectrum) because there are a set of angles corresponding to discrete paths which constructively interfere and make up the normal (natural) modes of the shallow water environment.

1.2 SOUND PROPAGATION MODELS

Sound propagation in the ocean is mathematically described by the wave equation, whose parameters and boundary conditions are descriptive of the ocean environment. There are essentially four types of models (computer solutions to the wave equation) to describe sound propagation in the sea: ray theory, the spectral method or fast field program (FFP), normal mode (NM) and parabolic equation (PE) [2]. All of these models allow for the fact that the ocean environment varies with depth. A model that also takes into account horizontal variations in the environment (i.e., sloping bottom or spatially variable oceanography) is termed range dependent. For high frequencies (a few kilohertz or above), ray theory is the most practical. The other three model types are more applicable and usable at lower frequencies (below a kilohertz). Here, we will confine the discussion to the normal mode model including its mild adiabatic range-dependent extension and the parabolic equation (see Appendix A).

1.2.1 The Wave Equation and Boundary Conditions

The wave equation for pressure in cylindrical coordinates with the range coordinates denoted by $\mathbf{r} = (x, y)$ and the depth coordinate denoted by z (taken positive downward) for a source free region of constant density ρ is

$$\nabla^2 p(\mathbf{r}, z, t) - \frac{1}{c^2} \frac{\partial^2 p(\mathbf{r}, z, t)}{\partial t^2} = 0, \tag{6}$$

where c is the sound speed in the wave propagating medium. The wave equation is most often solved in the frequency domain; that is, a frequency dependence of $exp(-i\omega t)$ is assumed to obtain the Helmholtz equation ($K \equiv \omega/c$),

$$\nabla^2 p(\mathbf{r}, z) + K^2 p(\mathbf{r}, z) = 0. \tag{7}$$

The most common plane interface boundary conditions encountered in underwater acoustics are described below: For the ocean surface there is the pressure release condition where the pressure vanishes,

$$p = 0. \tag{8}$$

The interface between the water column (layer 1) and an ocean bottom sediment (layer 2) is often characterized as a fluid-fluid interface. The continuity of pressure and vertical particle velocity at the interface yields the following boundary conditions in terms of pressure:

$$p_1 = p_2, \qquad \frac{1}{\rho_1} \frac{\partial p_1}{\partial z} = \frac{1}{\rho_2} \frac{\partial p_2}{\partial z}. \tag{9}$$

These boundary conditions applied to the plane wave fields in Fig. 4(a) yield the Rayleigh reflection coefficient given by Eq. 1.

The Helmholtz equation for an acoustic field from a point source with angular frequency ω is

$$\nabla^2 G(\mathbf{r}, z) + K^2(\mathbf{r}, z) G(\mathbf{r}, z) = -\delta^2(\mathbf{r} - \mathbf{r}_s)\delta(z - z_s); \quad K^2(\mathbf{r}, z) = \frac{\omega^2}{c^2(\mathbf{r}, z)}, \tag{10}$$

where the subscript "s" denotes the source coordinates. The range dependent environment manifests itself as the coefficient $K^2(\mathbf{r}, z)$ of the partial differential equation for the appropriate sound speed profile. The range dependent bottom type and topography appear as boundary conditions. The acoustic field from a point source, $G(\mathbf{r})$, is either obtained by solving the boundary value problem of Eq. 10 (spectral method or normal modes) or by approximating Eq. 10 by an initial value problem (ray theory, parabolic equation).

1.2.2 Normal Mode Model (NM)

For a range-independent environment, we assume a pressure field solution of Eq. 10 of the form

$$G(\mathbf{r}, z) = \frac{1}{2\pi} \int_{-\infty}^{\infty} d^2\mathbf{k} \; g(\mathbf{k}, z, z_s) \exp[i\mathbf{k}\cdot(\mathbf{r} - \mathbf{r}_s)], \tag{11}$$

which then leads to the equation for the depth dependent Green's function, $g(\mathbf{k}, z, z_s)$,

$$\frac{d^2 g}{dz^2} + [K^2(z) - k^2]g = -\frac{1}{2\pi}\delta(z - z_s). \tag{12}$$

We can solve Eq. 12 for g using a normal mode expansion of the form

$$\mathrm{g}(\mathbf{k}, z) = \sum a_n(\mathbf{k}) u_n(z), \tag{13}$$

where the quantities u_n are eigenfunctions of the following eigenvalue problem:

$$\frac{d^2 u_n}{dz^2} + \left[K^2(z) - k_n^2\right] u_n(z) = 0. \tag{14}$$

The eigenfunctions, u_n, are zero at $z = 0$, satisfy the local boundary conditions descriptive of the ocean bottom properties and satisfy a radiation condition for $z \to \infty$. They form an orthonormal set in a Hilbert space with weighting function $\rho(z)$, the local density. The range of discrete eigenvalues of Eq. 14 is given by the condition

$$\min[K(z)] < k_n < \max[K(z)]. \tag{15}$$

These discrete eigenvalues correspond to discrete angles within the critical angle cone in Fig. 5 such that specific waves constructively interfere. The mode functions form a complete set (for simplicity we omit discussion of the continuous spectrum though a good approximation is to use a set of discrete mode functions obtained from a waveguide extended in depth and terminated by a pressure release or rigid boundary)

$$\sum_{all\ modes} \frac{u_n(z) u_n(z_s)}{\rho(z_s)} = \delta(z - z_s), \tag{16}$$

and satisfy the orthonormality condition

$$\int_0^\infty \frac{u_m(z) u_n(z)}{\rho(z)} dz = \delta_{nm}, \tag{17}$$

where δ_{nm} is the Kronecker delta symbol. The eigenvalues k_n typically also have a small imaginary part α_n, which serves as the modal attenuation representative of all the losses in the ocean environment (see [2] for the formulation of normal mode attenuation coefficients).

Solving Eq. 10 using the normal mode expansion given by Eq. 13 yields (for the source at the origin).

$$G(r, z) = \frac{i}{4\rho(z_s)} \sum_n u_n(z_s) u_n(z) H_0^1(k_n r). \tag{18}$$

The asymptotic form of the Hankel function can be used in the above equation to obtain the well known normal mode representation of a cylindrical (axis is depth) waveguide:

$$G(r, z) = \frac{i}{\rho(z_s)(8\pi r)^{1/2}} \exp(-i\pi/4) \sum_n \frac{u_n(z_s) u_n(z)}{k_n^{1/2}} \exp(ik_n r). \tag{19}$$

Equation 19 is a far field solution of the wave equation and neglects the continuous spectrum ($k_n < \min[K(z)]$ of Ineq. 15) of modes. For purposes of illustrating the various portions of the acoustic field, we note that k_n is a horizontal wave number so that a "ray angle" associated with a mode with respect to the horizontal can be taken to be $\theta = cos^{-1}[k_n/K(z)]$. For a simple waveguide the maximum sound speed is the bottom sound speed corresponding to $\min[K(z)]$. At this value of $K(z)$, we have from Snell's Law $\theta = \theta_c$, the bottom critical angle. In effect, if we look at a ray picture of the modes, the continuous portion of the mode spectrum corresponds to rays with grazing angles greater than the bottom critical angle of Fig. 4(b) and therefore outside the cone of Fig. 5. This portion undergoes
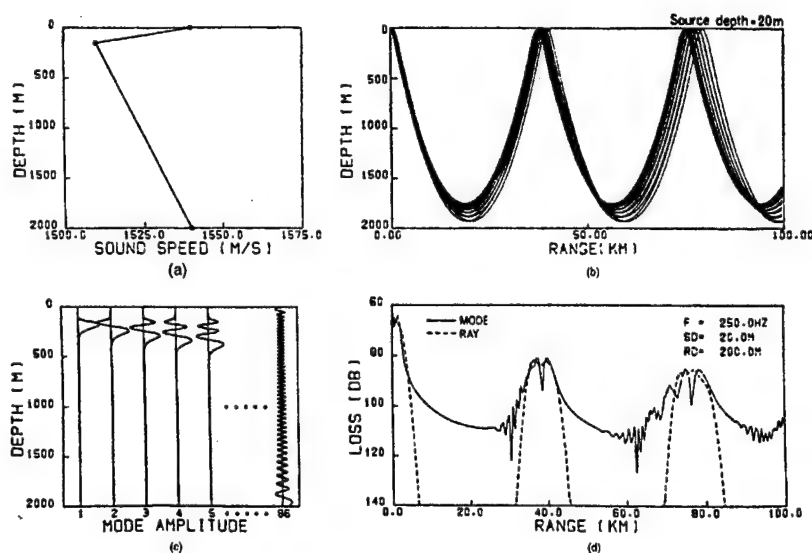
Figure 6: Ray and normal mode theory. (a) Sound speed profile (b) Ray trace (c) Normal modes (d) Propagation calculations.

severe loss. Hence, we note that the continuous spectrum is the near (vertical) field and the discrete spectrum is the (more horizontal, profile dependent) far field (falling within the cone in Fig. 5).

The advantages of the NM procedure are that: the solution is available for all source and receiver configurations once the eigenvalue problem is solved; it is easily extended to moderately range-dependent conditions using the adiabatic approximation; it can be applied (with more effort) to extremely range-dependent environments using coupled mode theory. However, it does not include a full representation of the near field.

1.2.3 Adiabatic Mode Theory

All of the range independent normal mode "machinery" developed for environmental ocean acoustic modeling applications can be adapted to mildly range dependent conditions using adiabatic mode theory. The underlying assumption is that individual propagating normal modes adapt (but do not scatter or "couple" into each other) to the local environment. The coefficients of the mode expansion, a_n in Eq. 13, now become mild functions of range, i.e., $a_n(\mathbf{k}) \rightarrow a_n(\mathbf{k}, \mathbf{r})$. This modifies Eq. 19 as follows:

$$G(\mathbf{r}, z) = \frac{i}{\rho(z_s)(8\pi r)^{1/2}} \exp(-i\pi/4) \sum_n \frac{u_n(z_s)v_n(z)}{\overline{k_n}^{-1/2}} \exp(i\overline{k_n}r). \tag{20}$$

where the range-averaged wave number (eigenvalue) is

$$\overline{k_n} = \frac{1}{r} \int_0^r k_n(r')\, dr', \tag{21}$$

and the $k_n(r')$ are obtained at each range segment from the eigenvalue problem Eq. 14 evaluated at the environment for that particular range along the path. The quantities u_n and v_n are the sets of modes at the source and the field positions, respectively.
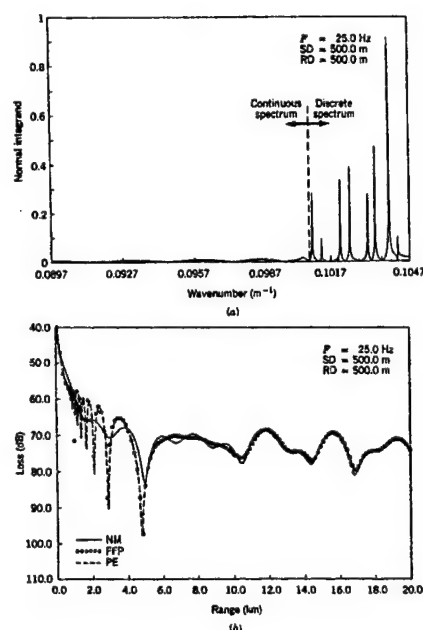
Figure 7: Relationship between FFP, NM and PE computations. (a) FFP Green's function from Eq. 12. (b) NM, FFP and PE propagation results showing some agreement in near field and complete agreement in far field.

Simply stated, the adiabatic mode theory leads to a description of sound propagation such that the acoustic field is a function of the modal structure at both the source and the receiver and some average propagation conditions between the two. Thus, for example, when sound emanates from a shallow region where only two discrete modes exist and propagates into a deeper region with the same bottom (same critical angle), the two modes from the shallow region adapt to the form of the first two modes in the deep region. However, the deep region can support many more modes; intuitively, we therefore expect the resulting two modes in the deep region will take up a smaller more horizontal part of the cone of Fig. 5 than they take up in the shallow region. This means that sound rays going from shallow to deep tend to become more horizontal which is consistent with a ray picture of downslope propagation. Finally, fully coupled mode theory for range dependent environments has been developed [3] but requires extremely intensive computation.

1.3 QUANTITATIVE DESCRIPTION OF PROPAGATION

All of the models described above attempt to describe reality and to solve in one way or another the Helmholtz equation. They therefore should be consistent and there is much insight to be gained from understanding this consistency. The models ultimately compute propagation loss which is taken as the decibel ratio (see Appendix B) of the pressure at the field point to a reference pressure, typically one meter from the source.

Figure 6 shows convergence zone type propagation for a simplified profile. The ray trace in Fig. 6(b) shows the cyclic focusing discussed in Section 1.1. The same profile is used to calculate the normal
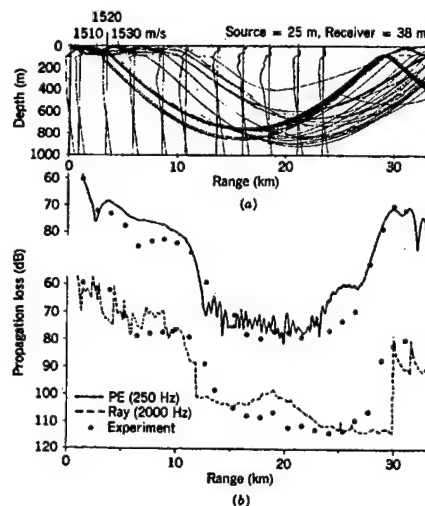
Figure 8: Model and data comparison for a range dependent case. (a) Profiles and ray trace for a case of a surface duct disappearing. (b) 250 Hz PE and 2 kHz Ray trace comparisons with data.

modes shown in Fig. 6(c) which when summed according to Eq. 19 yield the same cyclic pattern as the ray picture. Figure 6(d) shows both the normal mode (wave theory) and ray theory result. Ray theory exhibits sharply bounded shadow regions as expected whereas the normal mode theory, which includes diffraction, shows that the acoustic field does exist in the shadow regions and the convergence zones have structure.

Normal mode models sum the discrete modes which roughly correspond to angles of propagation within the cone of Fig. 5. The spectral (FFP) method can include the full field, discrete plus continuous, the latter corresponding to larger angles. The spectral model involves solving Eq. 12 numerically for a continuum of wavenumbers, k, without the normal mode expression of Eq. 13 (see Fig. 7(a)). Therefore, the consistency we expect between the normal mode and the spectral method and the physics of Fig. 5 is that the continuous portion of the spectral solution decays rapidly with range so that there should be complete agreement at long ranges between normal mode and spectral solutions. The Lloyd's mirror effect, a near field effect, should also be exhibited in the spectral solution but not the normal mode solution. These aspects are apparent in Fig. 7(b). The PE solution appears in Fig. 7(b) and is in good agreement with the other solutions but with some phase error associated with the average wavenumber that must be chosen in the split step method. The PE solution, which contains part of the continuous spectrum including the Lloyd mirror beams, is more accurate than the normal mode solution at short range; more recent PE results [27] can be made arbitrarily accurate in the forward direction.

Range dependent results [2] are shown in Fig. 8. A ray trace, a ray trace field result, a PE result and data are plotted together for a range dependent sound speed profile environment. The models agree with the data in general with the exception that the ray results predict too sharp a leading edge of the convergence zone.

Upslope propagation is modeled with the PE in Fig. 9. As the field propagates upslope, sound is dumped into the bottom in what appear to be discrete beams [4]. The flat region has three modes
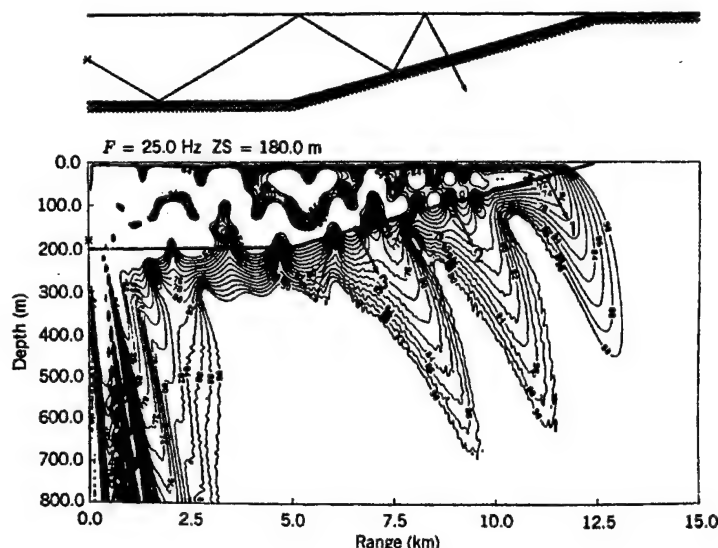
Figure 9: Relation between upslope propagation (from PE calculation) showing individual mode cutoff and energy dumping in the bottom, and a corresponding ray schematic.

and each is cut-off successively as sound propagates into shallower water. The ray picture also has a consistent explanation of this phenomenon. The rays for each mode become steeper as they propagate upslope. When the ray angle exceeds the critical angle the sound is significantly transmitted into the bottom. The locations where this takes place for each of the modes is identified by the three arrows.

2 Matched Field Processing

Spatial sampling of a sound field is usually done by an array of transducers, although the synthetic aperture array, in which a sensor is moved through space to obtain measurements in both the time and space domains, is an important exception. Spatial sampling is analogous to temporal sampling with the sampling interval replaced by the sensor spacing vectors. The Nyquist criterion requires that the sensor spacing be at least twice the spatial wavenumber of the measured sound field. Aliasing and signal reconstruction follow the same principles as for temporal data except that ambiguity can arise in the reconstructed wavenumber components due to symmetries in the array geometry. The simplest example of array processing is phase shading in the frequency domain (or time delay in the time domain) to search in bearing for a plane wave signal and is referred to as plane wave beamforming, or delay and sum beamforming in the time domain. This form of beamforming is discussed elsewhere and we will move on to a process referred to as matched field processing.

Matched field processing (MFP) [5] is the three-dimensional generalization of the conventional lower-dimensional plane wave beamformer. The one or two dimensions in the latter case are bearing and/or elevation and the matching is done to plane waves. Localization in this case refers to determining a direction. The generalized matched field beamformer matches the measured field at the array with replicas of the expected field for all source locations. These replicas are derived from propagation
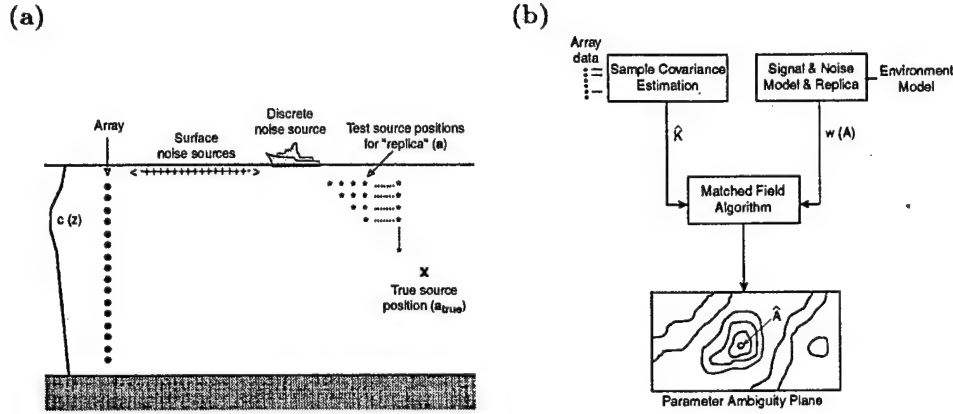
Figure 10: Matched field processing. (a) schematic of the procedure, (b) block diagram of the processor.

models as discussed above or in more detail in Ref. [2]. The unique spatial structure of the field permits localization in range, depth and azimuth depending on the array geometry and complexity of the ocean environment. The complex interference pattern of the acoustic field is a function of the source location and this pattern can be "matched." In terms of rays we can say that the refractive properties of the waveguide generate a pattern of arrival angles that can also be matched. The process is shown schematically in Fig. 10. The process consists of systematically placing a test point source at each point of a search grid, computing the acoustic field (replicas) at all the elements of the array and then correlating this modeled field with the data from the real point source whose location is unknown. When the test point source is collocated with the true point source, the correlation will be a maximum. The two main factors which limit performance of MFP are noise, natural and man made, and the ability to accurately model the ocean acoustic environment.

Now construct the replica field, $\mathbf{w}(\mathbf{a})$ on the array for each candidate position, $\mathbf{a}$ from one of the numerical solutions to the acoustic wave equation, Eq. 10. The replica vector is normalized, i.e., it has unit length, so that the output of the processor is the source strength,

$$\mathbf{w}(\mathbf{a}) = \frac{G(\mathbf{a})}{|G(\mathbf{a})|}, \tag{22}$$

where $G(\mathbf{a})$ is the vector whose ith element is the solution to the waveguide equation, e.g., Eq. 19, at the field (hydrophone) position $(\mathbf{r}, z) = (\mathbf{r}_i, z_i)$ for a source at $\mathbf{a}$.

Rather than find just the direction of the source from the array, we can search for its actual location by matching the received data, $\mathbf{d}(\mathbf{a}_{true})$ from the true source location against solutions of the wave equation. The matching process is then similar to plane wave beamforming with the plane waves being replaced by solutions of the wave equation. The output of this matched field process, denoted $S(\mathbf{a})$, at each point in space $\mathbf{a}$ is given by

$$S(\mathbf{a}) = |\mathbf{w}^\dagger(\mathbf{a})\mathbf{d}(\mathbf{a}_{true})|^2. \tag{23}$$

This equation can be rewritten in terms of the cross-spectral density matrix of the array data, $\mathbf{K}(\mathbf{a}_{true}) = \mathbf{d}(\mathbf{a}_{true})\mathbf{d}^\dagger(\mathbf{a}_{true})$,

$$S(\mathbf{a}) = \mathbf{w}^\dagger(\mathbf{a})\mathbf{K}(\mathbf{a}_{true})\mathbf{w}(\mathbf{a}). \tag{24}$$
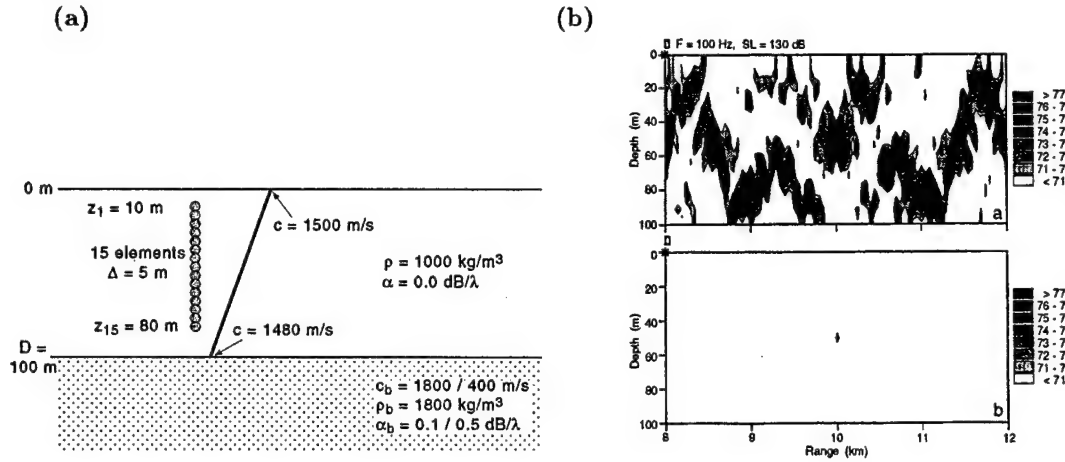
Figure 11: Matched field processing. (a) Environment and geometry for shallow water example. (b) Matched-field ambiguity surfaces for a 130 dB source (r_s=10 km, z_s=50 m). Bartlett (top) and MVDP (bottom).

There are an assortment of interesting issues concerning the actual measurement of cross-spectral density matrix, particularly when adaptive processing is utilized. These issues are addressed in the chapter by Baggeroer.

The peak of the output of the beamformer, $S(\mathbf{a})$, is at $\mathbf{a}_{true}$. $S(\mathbf{a})$ is also referred to as the ambiguity function (or surface) of the matched field processor because it also contains ambiguous peaks which are analogous to the sidelobes of a conventional plane wave beamformer. Sidelobe suppression can often be accomplished by adaptive processing which is also discussed in the Baggeroer chapter. Here we write down the form of one of the adaptive processors: the minimum variance distortionless processor

$$S_{MVDP}(\mathbf{a}) = [\mathbf{w}^{\dagger}(\mathbf{a})\mathbf{K}^{-1}(\mathbf{a}_{true})\mathbf{w}(\mathbf{a})]^{-1}, \tag{25}$$

where again we note from above that there are measurement issues associated with estimating an invertible cross spectral density matrix.

A vertical receive array simulation example of the Bartlett and MVDP MFP processors for an ocean acoustic waveguide with a high signal to noise ratio is shown in Fig. 11. In MFP, mismatch between replicas, that are derived from a usually incomplete knowledge of the environment, and observed data is a significant problem that has received much attention. Matched field tomography (MFT)searches for the environmental parameters controlling the propagation (for example the index of refraction which may be a spatially dependent coefficient of the wave equation) rather than source location. As with the case of plane wave beamforming, there are an assortment of processors that can be used for MFP/MFT [5]

There have been two approaches to deal with environmental mismatch in MFP. The first has been to constructing processors which are tolerant to environmental uncertainty [6, 7, 8]. These processors trade resolution for lack of precise knowledge of the environment. The second approach is focalization [9] which uses nonlinear optimization methods to simultaneously search for the environment and the source position. All of these methods have limitations, but under various conditions they have been successfully applied to experimental data.

3   Phase Conjugation in the Ocean

Phase conjugation (PC) [10] and its time domain equivalent referred to as a time reversal mirror (TRM) is a process that has been first demonstrated in nonlinear optics. The time reversal mirror in ultrasonics [11, 12] is the subject of Ch. ???. Aspects of phase conjugation as applied to underwater acoustics also have been explored recently [13, 14, 15, 16]. The Fourier conjugate of phase conjugation is time reversal; implementation of such a process over a finite spatial aperture results in a "time reversal mirror." This section will begin with a description of the basic theory and implementation in the ocean based on the ocean acoustics discussion above. This will be followed by a discussion of some of the more complex issues associated with the real ocean such as fluctuations, etc. Some of the material given below will overlap and supplement Ch. ???.

3.1   Basic Properties of Phase Conjugation

Phase conjugation takes advantage of reciprocity which is a property of wave propagation in a static medium and is a consequence of the invariance of the linear lossless wave equation to time reversal. In the frequency domain, time reversal corresponds to conjugation invariance of the Helmholtz equation. The property of reciprocity allows one to retransmit a time reversed version of a multipath dispersed probe pulse back to its origin, arriving there time reversed, with the multipath structure having been undone [17, 18]. This process is equivalent to using the ocean as a matched filter since the probe pulse arrival has embedded in it the transfer function of the medium. This process can be extended further by receiving and retransmitting the probe signal with a source-receive array. Depending on the spatial extent of the array, the above process results in some degree of spatial focusing of the signal at the origin of the probe signal.

A time reversal mirror (TRM) can therefore be realized with a source-receiver array. The incident signal is received, time reversed and transmitted from sources contiguous with the receiving hydrophones. The time reversal can be accomplished in a straightforward way, for example, by using the rewind output of an analog tape recorder or by a simple program that reverses a digitized segment of a received signal.

Phase conjugation or the implementation of a TRM in the ocean will be shown to be related to matched field processing (MFP) which requires detailed knowledge of the environment. Phase conjugation is an environmentally self-adaptive process which may therefore have significant applications to localization and communications in complicated ocean environments. Though the "effective" ocean environment must remain static over the turn around time of the PC process, ocean variability on time scales shorter than the turn around time might be compensated for with feedback algorithms. However, an understanding of relevant ocean time scales vis a vis the stability of the PC process will be required.

As noted earlier, phase conjugation in the ocean shares many features in common with ultrasonic time reversal. These general aspects will be discussed first and then those aspects that demand treatment of the ocean waveguide will be covered. The generic phase conjugation focusing experiment is depicted in Fig. 12. A point acoustic source, denoted the "probe source" transmits a signal which is received by the elements of an array capable of both reception and transmission (the "source-receiver array", or "SRA"). The signal received by each element is time-reversed and retransmitted on the *same* element (or perhaps on a nearby source element if the receiving elements are unsuited as acoustic
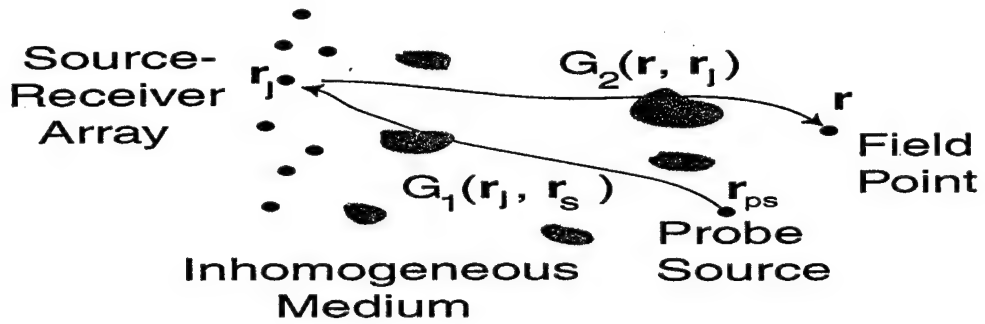
Figure 12: Schematic of the generic phase conjugation focusing experiment.

sources). The field produced by the array approximates a time-reversed version of the probe source field, consequently it focuses at the location of the probe source.

3.1.1 Idealized Arrays

In order to assess the degradation in focusing due to environmental effects, it is helpful to have a reference point for comparison. Thus, we will first consider ideal arrays capable of providing the sharpest possible focus. While one might think of the ideal case as producing a simple time-reversed version of the field due to the probe source, this ideal is unreachable, even in principle. To see this, consider a point probe source, which produces a field that approaches infinity as one approaches the source location. This infinite field does not satisfy the source-free wave equation at the source location, therefore it is impossible to produce such a field using an array whose elements are at a distance from the source location.

These considerations lead to the question, how sharp can the focus of the time-reversed field be? It is useful to first consider the ideal case, in which a continuous SRA *surrounds* a probe source, as shown in Fig. 13.

The probe source, situated at the location $\mathbf{r}_{ps}$ emits a time-harmonic field of angular frequency ω. We will take the source to have unit strength, obeying the inhomogeneous Helmholtz equation

$$\nabla^2 G_\omega(\mathbf{r}, \mathbf{r}_{ps}) + k(\mathbf{r})^2 G_\omega(\mathbf{r}, \mathbf{r}_{ps}) = -\delta(\mathbf{r} - \mathbf{r}_{ps}) \quad . \tag{26}$$

Note that this Green's function incorporates all the complexity of the problem at hand. That is, it satisfies appropriate boundary conditions such as those at the sea surface and bottom and includes all the effects of inhomogeneity in the sound speed in the position-dependent wavenumber $k(\mathbf{r}) = \omega/c(\mathbf{r})$. At a general point $\mathbf{r}'$ on its surface, the ideal SRA receives the field $G_\omega(\mathbf{r}', \mathbf{r}_{ps})$ of the probe source, conjugates it, and retransmits to a point $\mathbf{r}$ in the interior according to Huygen's principle as embodied in the Helmholtz-Kirchhoff integral [30]. The resulting field at $\mathbf{r}$ is
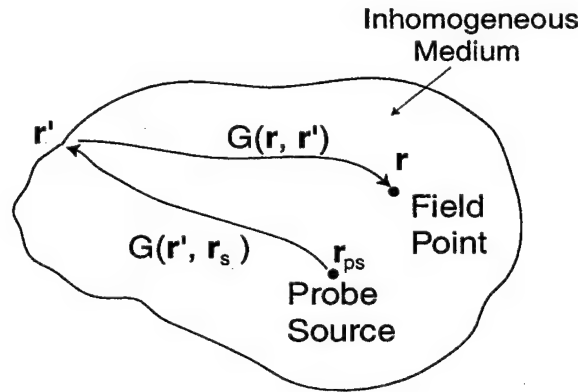
Figure 13: Schematic of ideal, closed source-receiver array (SRA).

$$P_{pc}(\mathbf{r};\omega) = \int \left[G_\omega(\mathbf{r},\mathbf{r}') G_\omega^*(\mathbf{r}',\mathbf{r}_{ps}) + \nabla G_\omega(\mathbf{r},\mathbf{r}') \cdot \nabla G_\omega^*(\mathbf{r}',\mathbf{r}_{ps}) \right] dS' \quad . \tag{27}$$

As Porter [30] has shown, in the lossless case (that is, when $k(\mathbf{r})$ is real), the field produced by the ideal array can be expressed exactly as

$$P_{pc}(\mathbf{r};\omega) = 2i\Im m\{G_\omega(\mathbf{r},\mathbf{r}_{ps})\} \quad . \tag{28}$$

By taking the imaginary part of Eq. 26 it can be seen that $P_{pc}(\mathbf{r},\mathbf{r}_{ps};\omega)$ is a solution of the sourceless (homogeneous) Helmholtz equation. Thus, it is seen that the ideal SRA produces a field which is similar to the original field, but is source-free in the focus region, as it must be. The most remarkable aspect of this ideal case is the focus field is independent of the shape and location of the closed array, as long as it surrounds the original source. We will see that this ideal behavior has implications in more practical situations.

How good is the ideal focus? In the case where the medium is homogeneous in the vicinity of the original source and in which backscattering due to boundaries and inhomogeneities produces a negligible field near the original source, the original field can be approximated by the free-space Green's function,

$$G_\omega(\mathbf{r},\mathbf{r}_{ps}) \approx \frac{exp(ik|\mathbf{r} - \mathbf{r}_{ps}|)}{4\pi|\mathbf{r} - \mathbf{r}_{ps}|} \quad . \tag{29}$$

While this field is singular at $\mathbf{r} = \mathbf{r}_{ps}$, its imaginary part is not, as shown in Fig 14. It can be seen from the figure that the ideal focus has a width comparable to the wavelength. This ideal is not generally realized in more practical situations. Note that the focus field is oscillatory. It is, in fact, a standing wave created by the interference of waves launched from all directions, since the ideal SRA surrounds the focus.
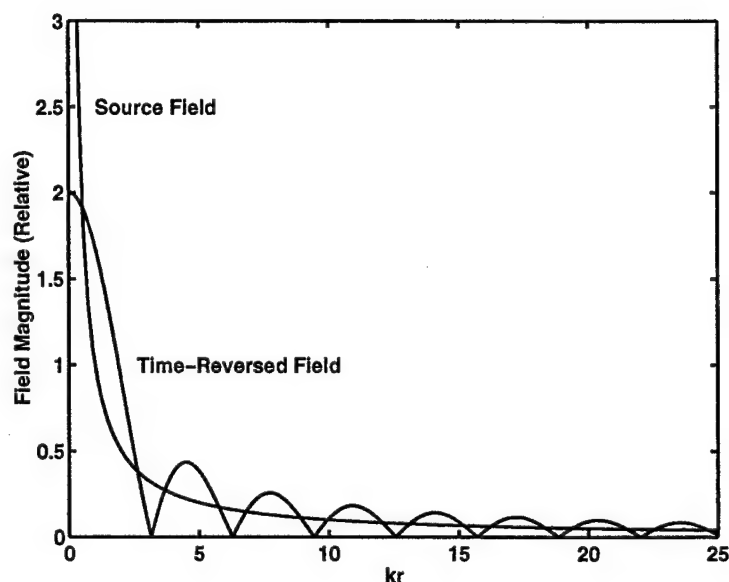
3.1.2 The open array

Figure 14: Comparison of Source and Ideal Focus Fields

In more realistic cases, the array will not be closed and will not surround the original source. The ideal array provides insight into such cases, as one can, as a thought experiment, divide the closed SRA into two parts, as in Fig. 15, the smaller of these parts representing an actual two-dimensional SRA. Consider deforming this array, while leaving the other portion undeformed. We know from the previous result that the focus field will not change as a result of this deformation. The focus field in this case is the sum of the fields from the two parts, and, as one part of the array is fixed, its contribution to the field must be fixed as well. It follows that the field of the smaller part must be unchanging, too. Thus, an ideal open two-dimensional SRA should display an interesting invariance property: Its focus field will be independent of deformations of the array provided the outer edge of the array is held fixed. Of course, this array is rather special; it is continuous and employs both the incident field and its normal derivative. Nevertheless, we shall see that this invariance survives at least as an approximation in realistic situations.

It is possible to extract an additional useful piece of information from this example. Consider an infinite, planar SRA in a homogeneous acoustic medium. It can be considered as one-half of a closed array formed from two planes placed symmetrically with respect to the probe source. In the plane parallel to the arrays and passing through the source, symmetry dictates that each array produces the same field, thus the infinite planar SRA must produce a $sin(kR)/kR$ field in the plane through the source, where R is the distance from the source.

3.1.3   The discrete array

In practice, creating an array to approximate even an open version of the array represented by Eq. 13 is very difficult, as this array must be capable of sensing both the incident field and its normal derivative. Furthermore, it must include both monopole sources (to produce $G(\mathbf{r}, \mathbf{r}', \omega)$), and dipole sources (to
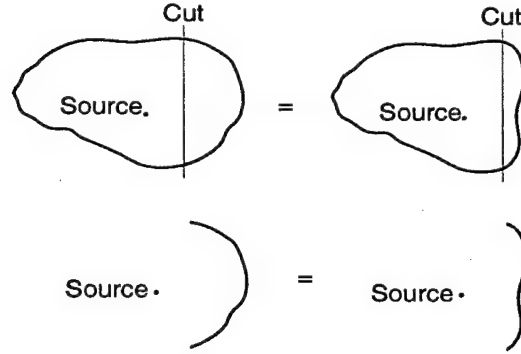
Figure 15: Demonstration of shape invariance of ideal open arrays.

produce $\nabla G(\mathbf{r}, \mathbf{r}', \omega))$. The general problem of using arrays with various combinations of monopole and dipole sources is discussed by Cassereau and Fink [31]. In low-frequency underwater acoustics, arrays are usually composed of discrete elements that are omnidirectional or nearly so. Such arrays are more accurately represented by a set of discrete monopole receivers/sources as illustrated in Fig. 12.

In the harmonic case, such an array produces the following field in response to a point probe source of unit strength.

$$P_{pc}(\mathbf{r};\omega) = \sum_{j=1}^{J} G_{2,\omega}(\mathbf{r},\mathbf{r}_j) G_{1,\omega}^*(\mathbf{r}_j,\mathbf{r}_{ps}) \ . \tag{30}$$

The sum is over the J elements of the SRA whose position vectors are denoted $\mathbf{r}_j$. Propagation from the probe source to the SRA is described by the Green's function $G_{1,\omega}(\mathbf{r}_j, \mathbf{r}_{ps})$, while propagation from the SRA to the field point is described by $G_{2,\omega}(\mathbf{r}, \mathbf{r}_n)$. The subscripts 1 and 2 allow for the possibility that time variation of the ocean might cause changes in the Green's function between the probe and phase-conjugate transmission cycles. During either propagation cycle, the ocean is assumed to be "frozen" in the sense that it behaves as a time-invariant linear system. In this view, the Green's function is the frequency-dependent system transfer function for acoustic propagation between any two points in the ocean. It instructive to consider the focus field at the location of the probe source. Suppressing the subscripts 1 and 2 in Eq. 30, the field at $\mathbf{r} = \mathbf{r}_{ps}$ is

$$P_{pc}(\mathbf{r}_{ps};\omega) = \sum_{j=1}^{J} |G_\omega(\mathbf{r}_{ps},\mathbf{r}_j)|^2 \ . \tag{31}$$

In Eq. 31, reciprocity has been used in the form $G_\omega(\mathbf{r}_{ps}, \mathbf{r}_j) = G_\omega(\mathbf{r}_j, \mathbf{r}_{ps})$, which neglects gradients in density. The field at the focus is a sum of positive terms, that is, the transmissions from each element of the SRA arrive exactly in phase at the probe source location. Even though each term in this sum is likely to have complicated dependence on frequency, ω, owing to modal interference (equivalently, owing to multipath propagation), the sum will tend to have less severe frequency dependence than the
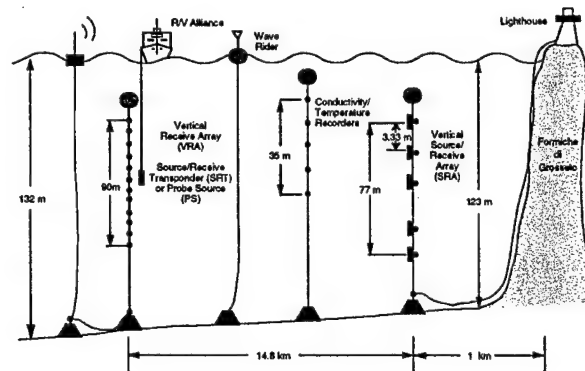
Figure 16: Experimental setup of phase conjugation experiment.

individual terms. This is because each element of the SRA is subject to different modal interference, with destructive interference tending to occur at different frequencies for each element. This lack of frequency dependence at the source location implies that a time-reversed pulse will suffer little multipath distortion at the focus. See Sec. 3.2.2 for a discussion of this matter in the time domain. Note that the field at the focus is proportional to the sum over the SRA of the squared probe source pressure at each element. If the SRA samples the nearly the entire water depth, this sum will tend to be stable and independent of details of propagation in the intervening medium, as the sum is a measure of the total power propagating through the waveguide. Thus, if one imagines perturbing the environment by altering the seafloor roughness or by introducing slight random changes in the sound speed of the medium, one would not expect the field value at the focus to change appreciably. This is another indication of the robust nature of phase-conjugate focusing.

3.2 Background Theory and Simulation for Phase Conjugation/TRM in the Ocean

The theory of phase conjugation *vis a vis* ocean acoustics already has been presented [19, 20]. Here we briefly review salient issues using the basic geometry of an ocean TRM experiment [19, 21] as shown schematically in Fig. 16. The figure also indicates the types of environmental measurements that were made. The TRM was implemented by a 77 m source-receiver array (SRA) in 125 m deep water The SRA consisted of 20 hydrophones with 20 contiguously located sources with a nominal resonance frequency of 445 Hz. The sources were operated at a mean nominal 165 dB source level. The received signals from a probe source (PS) were digitized, time reversed and after being converted back to analog form, retransmitted. A vertical 46 element receive array (VRA) spanning 90 m located initially 6.3 km from the SRA at the PS range.
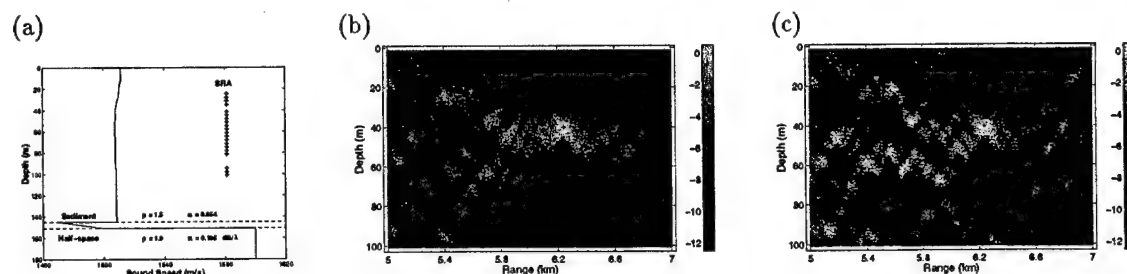
(a) (b) (c)

Figure 17: Single frequency simulation of phase conjugation for the geometry of Fig. 16 for a probe source located at a depth of 40 m and a range of 6.3 km. (a) Sound speed profile. The density, ρ and attenuation, α (in dB/wavelength) of the bottom two layers are also given. (b) Simulation for a 20 element SRA. Note the sharp focus in depth. (c) Simulation for only the bottom 10 elements of the SRA.

3.2.1 Harmonic Point Source

For a unit harmonic source of angular frequency ω located at $(\mathbf{r}_{ps}, z_{ps})$, the pressure field, $G_\omega(R; z_j, z_{ps})$, at the j-th receiver element of the SRA from the point source PS in Fig. 16 is determined from Eq. 19,

$$G_\omega(r; z, z_{ps}) = \frac{i}{\rho(z_{ps})(8\pi r)^{1/2}} \exp(-i\pi/4) \sum_n \frac{u_n(z_{ps})u_n(z)}{k_n^{1/2}} \exp(ik_n r). \tag{32}$$

For a vertical line of discrete sources, Eq.30 (with the subscripts 1 and 2 dropped, because time dependence of the medium is neglected), takes the form

$$P_{pc}(r, z; \omega) = \sum_{j=1}^{J} G_\omega(r; z, z_j) G_\omega^*(R; z_j, z_{ps}), \tag{33}$$

where R is the horizontal distance of the SRA from PS and r is the horizontal distance from the SRA to a field point. We can implement Eq. 33 with propagation models other than the normal mode example we are using. For mildly range-dependent environments, we can use the adiabatic mode theory for $G_\omega(r; z, z_j)$ described in Section 1.2.3. For more highly range-dependent environments, the parabolic equation model is not only more appropriate, it is intuitively suitable in the sense that it uses a range marching algorithm; hence, it is a direct implementation of back propagation. This model is described in Appendix A and we note here that it has recently been applied to some interesting medical ultrasonics problems [22].

Note that the magnitude squared of the right hand side (r.h.s.) of Eq. 33 is the unnormalized (see Eq. 22) ambiguity function of the matched field processor of Eq. 23 where the data, d, is given by $G_\omega(R; z_j, z_{ps})$ and the unnormalized replica field by $G_\omega(r; z, z_j)$. In effect, the process of phase conjugation is an implementation of matched field processing where the ocean itself is used to construct the replica field. Or, alternatively, matched field processing simulates the experimental implementation of phase conjugation in which a source/receive array is used. To demonstrate that $P_{pc}(r, z)$ focuses at the position of the probe source, (R, z_{ps}), we simply substitute Eq. 32 into Eq. 33 which specifies that we sum over all modes and array sources

$$P_{pc}(r, z; \omega) \approx \sum_m \sum_n \sum_j \frac{u_m(z)u_m(z_j)u_n(z_j)u_n(z_{ps})}{\rho(z_j)\rho(z_{ps})\sqrt{k_m k_n r R}} \exp i(k_m r - k_n R). \tag{34}$$

For an array which substantially spans the water column and adequately samples most of the modes, we may approximate the sum of sources as an integral and invoke orthonormality as specified by Eq. 17. Then the sum over j selects out modes $m = n$ and Eq. 34 becomes

$$P_{pc}(r, z; \omega) \approx \sum_m \frac{u_m(z)u_m(z_{ps})}{\rho(z_{ps})k_m\sqrt{rR}} \exp ik_m(r - R). \tag{35}$$

The individual terms change sign rapidly with mode number. However, for the field at PS, $r = R$, the closure relation of Eq. 16 can be applied approximately (we assume that the k_n's are nearly constant over the interval of the contributing modes) with the result that $P_{pc}(r, z) \approx \delta(z - z_{ps})$. Figure 17(b) is a simulation of the phase conjugation process using Eq. 33 for a probe source at 40 m depth and at a range of 6.3 km from a 20 element SRA as specified in Fig. 16 verifying the above discussion. Measured range-dependent bathymetry, bottom properties and sound speed profile were used as the input to an adiabatic mode model (section 1.2.3). Notice that the focusing in the vertical is indicative of the closure property of the modes. As a matter of fact, for an SRA with substantially fewer elements, we see that the focusing still is relatively good. For example, Fig. 17(c) also shows a result for the bottom 10 elements of the SRA which are below the thermocline.

3.2.2 Pulse Excitation

In the actual experiments, a 50 ms pure-tone pulse with center frequency 445 Hz was used for the probe transmission. We can Fourier synthesize the above results to examine phase conjugation for pulse excitation. Here, in the context of this experiment, we remind the reader that phase conjugation in the frequency domain is equivalent to time reversal in the time domain. The jth element of the SRA receives the following time-domain signal, given by Fourier synthesis of the solution of Eq. 28,

$$P(R, z_j; t) = \int G_\omega(R; z_j, z_{ps})S(\omega)e^{-i\omega t}d\omega , \tag{36}$$

where $S(\omega)$ is the Fourier transform of the probe source pulse. This expression incorporates all waveguide effects, including time elongation due to multipath propagation. For convenience, take the time origin such that $P(R, z_j; t) = 0$ outside the time interval $(0, \tau)$. Then the time-reversed signal that will be used to excite the *jth* transmitting element of the SRA is $P(R, z_j; T - t)$ such that $T > 2\tau$. This condition is imposed by causality; the signal has to be completely received before it can be time reversed. Then

$$P(R, z_j; T - t) = \int G_\omega(R; z_j, z_{ps})S(\omega)e^{-i\omega(T-t)}d\omega = \int [G_\omega^*(R; z_j, z_{ps})e^{i\omega T}S^*(\omega)]e^{-i\omega t}d\omega , \tag{37}$$

where the sign of the integration variable, ω, has been reversed and the conjugate symmetry of the frequency-domain Green's function and probe pulse has been used. The quantity in brackets in Eq. 37 is the Fourier transform of the signal received by the *jth* SRA receiver element after time reversal and time delay. Hence there is an equivalence of time reversal and phase conjugation in their respective time and frequency domains.

Noting that the bracketed quantity in Eq. 37 is the frequency domain representation of the signal retransmitted by the *jth* element of the SRA, Fourier synthesis can be used to obtain the time-domain
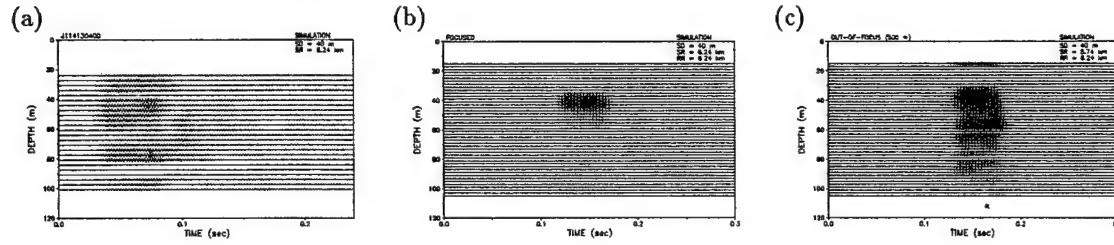
Figure 18: Simulation of a 445 Hz, 50 ms transmitted pulse for the geometry in Fig. 12 for a probe source located at a depth of 40 m. (a) Pulse received on the SRA at range of 6.3 km from PS. There is a temporal dispersion of about 75 ms and significant energy throughout the water column. (b) The focus of the time reversed pulse at the VRA. There is pulse compression back to the original transmitted 50 ms duration as well as spatial focusing in depth. (c) Vertical and temporal distribution for a pulse 500 m outbound of PS (the VRA is at the same location but PS is 500 m closer to the SRA).

representation of the field produced by the TRM. Using Eq. 33,

$$P_{pc}(r,z;t) = \sum_{j=1}^{J} \int G_\omega(r,z,z_j)G_\omega^*(R,z_j;z_{ps})e^{i\omega T}S^*(\omega)e^{-i\omega t}d\omega \ . \tag{38}$$

This expression can be used to show that the TRM produces focusing in time as well as in space. Focusing in time occurs because a form of matched filtering occurs. To understand this, examine the TRM field at the focus point (that is, take $r = R$, $z = z_{ps}$ in Eq. 38). Neglecting density gradients, reciprocity allows the interchange $G_\omega(R,z_{ps},z_j) = G_\omega(R,z_j,z_{ps})$. Then the time-domain equivalent of Eq. 38 is

$$P_{pc}(r,z;t) = \frac{1}{(2\pi)^2} \int \sum_{j=1}^{J} \left[\int G_{t'+t''}(R,z_j,z_{ps})G_{t'}(R,z_j,z_{ps})dt' \right] S(t'' - t + T)dt'' \ , \tag{39}$$

where the time-domain representations of the Green's function and probe pulse are used. Note that the Green's function is correlated with itself. This operation is matched filtering, with the filter matched to the impulse response for propagation from the probe source to the jth SRA element. This operation gives focusing in the time-domain, that is, it reduces the time elongation due to multipath propagation [17]. The sum over array elements is a form of spatial matched filtering, analogous to that employed in the matched field processor. In addition, this sum further improves temporal focusing as the temporal sidelobes of the matched filters for each channel tend to average to zero which also is analogous to broadband matched-field processing results [23]. Finally, note that the integral over t'' in Eq. 39 is a convolution of each matched-filtered channel impulse response with the time reversed and delayed probe pulse. As a consequence, this pulse is *not* matched filtered, for example, a linear FM up-sweep will appear as a down-sweep at the focus and will not be compressed.

Figure 18(a) shows a simulation for a 50 ms rectangular pulse with center frequency 445 Hz for the same geometry used in Fig. 17(a) as received at the SRA and Fig. 18(b) shows the pulse as transmitted to a plane at a range of 6.3 km, the range of PS. Four sources were excluded from the simulation because these phones were not used in the experiment. Note the temporal focusing; that is, the 50 ms pulse disperses to about 75 ms at the SRA but the time reversed pulse received at the VRA is compressed
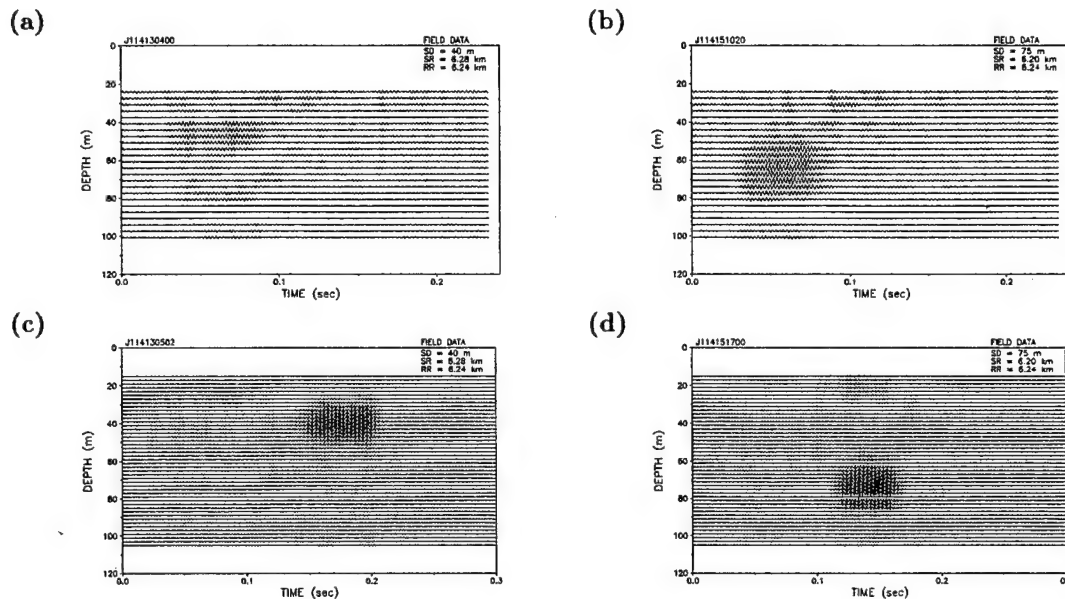
(a)

(b)

(c)

(d)

Figure 19: Experimental results for probe source PS and VRA at same range. (a) The pulse data received on the SRA for PS at depth of 40 m. (b) The pulse data received on the SRA for PS at depth of 75 m. (c) The data received on the VRA from the time reversed transmission of pulses shown in (a). The VRA is 40 m inbound from the focus as determined by DGPS. (d) The data received on the VRA from the time reversed transmission of pulse shown in (b). The VRA is 40 m outbound from the focus as determined by DGPS.

(focused) to 50 ms as opposed to exhibiting even further time dispersion. On the other hand Fig. 18(c) shows a pulse 500 m outbound of PS (i.e., the VRA is at the same location but PS is 500 m closer to the SRA). The pulse is not spatially focused and it is temporally more diffuse than the result for the focal spot.

3.2.3   Properties of the Focal Region

The TRM focus is robust, provided the SRA adequately samples the field in the water column. First, the focus tends to depend primarily on the properties of the ocean near the focus and tends to be independent of (the possibly range-dependent) properties of the medium between the SRA and the focus. Temporal changes in the medium due to, for example, surface waves and internal waves degrade the focus, but this degradation will be tolerable if the average (or coherent) Greens function is not severely reduced by these time variations. Generally, the shape of the focus is approximated by the field that a point source placed at the focus generates after non-propagating modes are subtracted. Thus, if absorption or scattering tends to eliminate high-order modes, the focus will be comprised of the remaining lower order modes and will be relatively broader. Very roughly, the vertical width of the focus will be equal to the water depth (or depth of the duct) divided by the number of contributing modes if the sound speed (in the duct) is not strongly dependent upon depth.

The TRM focus is also robust with respect to array shape [13] provided the shape does not change
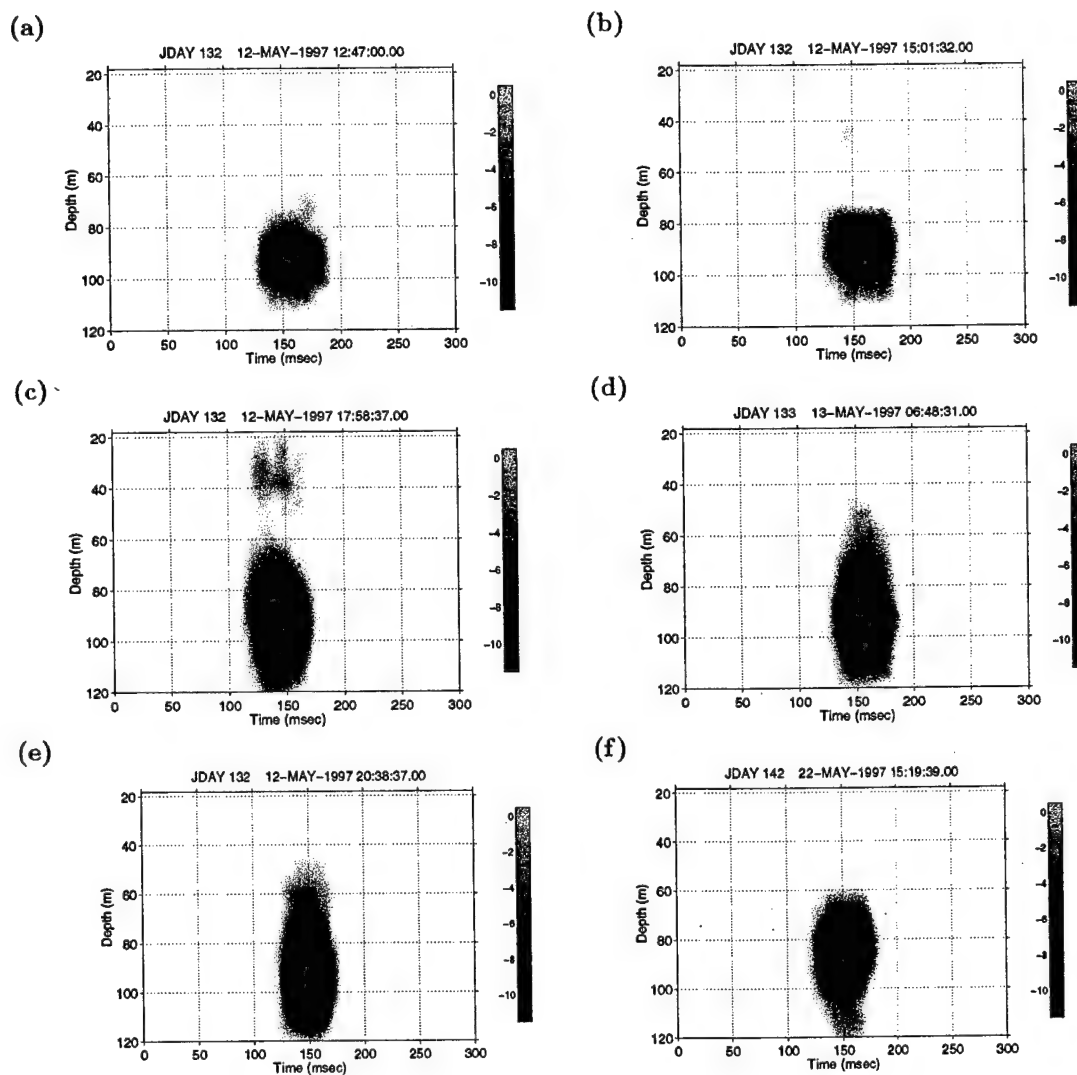
Figure 20: Experimental results for 50-ms, 445 Hz center frequency probe source (PS) at 81 m depth and various ranges, R, between the PS and the source-receive array (SRA). (a) R=4.5 km. (b) R=7.7 km. (c) R=15 km. (d) R=20 km. (e) R=30 km. (f) R=15 km. The vertical receive array (VRA) is within 60 m of the PS. Both the VRA and PS were suspended from the ALLIANCE except (f) which was from a rf-telemetered VRA at 15 km range in other run.
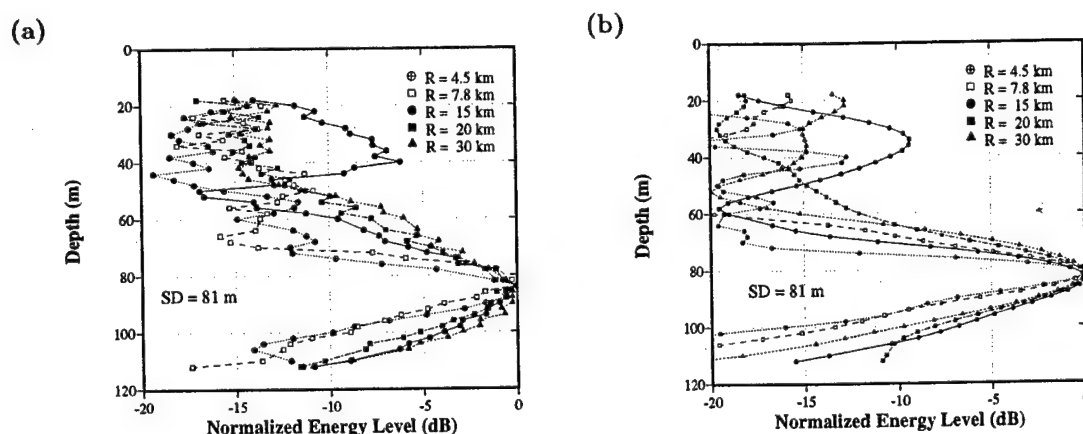
(a) (b)

Figure 21: The energy over a 0.3-s time window of the pulse received on VRA as a function of depth for various ranges. The depth of the probe source was 81 m. (a) Experimental results. (b) Simulation results. Note the sidelobe at around 40 m depth and 15 km range in both cases.

between the probe reception and time-reversed transmission. This property makes it unnecessary to know the exact shape of the TRM array and offers a considerable advantage over conventional beamforming. The focal properties are discussed in detail in Sect 4.

3.2.4 Variable Range Focusing

The time-reversal mirror technique has been extended to refocus at ranges other than that of the probe source [20]. The technique involves retransmitting the data at a shifted frequency according to the desired change in focal range, such that

$$(\Delta\omega/\omega) = \beta\,(\Delta R/R),\tag{40}$$

where the invariant β is determined by the properties of the medium. Typically, β is approximately equal to 1 in a large class of acoustic waveguides, which means that a 5% increase in frequency results in a 5% increase in focal range. On the other hand, $\beta \approx -3$ for a surface sound channel or in a waveguide with a deeply submerged channel axis. In this case, retransmitting frequency should be decreased to increase the focal range. The frequency shift can be implemented easily in near real-time by a FFT bin shift prior to retransmission. Recently, variable focusing in range has been applied to medical ultrasonics in free space [22].

3.3 Implementation of a Time Reversal Mirror in the Ocean

Two experiments [19, 21] were conducted by the SACLANT Undersea Research Centre (Dr. Tuncay Akal was the overall Chief Scientist of the experiments) and the Marine Physical Laboratory of Scripps. An assortment of runs was made to examine the structure of the focal point region and the temporal stability of the process. The TRM process was successfully demonstrated out to a range of thirty km in these experiments. Here we will be reporting on some of the results. (note that range refers to the distance from the SRA):

3.3.1 Demonstration of TRM in the Ocean

In the first experiment he vertical receive array VRA was deployed at a range, determined by DGPS, of 6.24 km from the SRA and the probe source PS was deployed at two different depths, 40 m and 75 m. Figure 19 shows the pulse as received on the SRA and VRA for both source depths. The data at the SRA is a combination of signal and noise. A 233 ms window was digitized and time reversed for transmission to the VRA. When the VRA and PS have the same range (experimentally within 40 m by a DGPS measurement) to the SRA, we see the focusing as predicted in Section 3.1 for a probe source at 40 m depth and similar results for a probe source at 75 m depth. Clearly, we have implemented a time reversal mirror focusing at the range and depth of the probe source.

In the second experiment, the probe source was deployed out to a range of 30 km. Figure 20 shows the results for PS at an 81-m depth for five different ranges from the SRA: 4.5, 7.7, 15, 20, and 30 km. As expected, the temporal focus remain compact while the spatial focus broadens with range due to mode stripping. The latter can be seen more quantitatively in Fig. 21(a). Simulations, shown in Fig. 21(b), using the measured environment confirm that the focal structure is consistent with the above theory.

To summarize, the TRM is still quite effective at 30 km, particularly for a deep probe source in the stable part of the water column. The focal region has a vertical extent of about 25 m (3 dB down from the peak) at a range of 30-km, which corresponds to 20% of the waveguide thickness at a range of about 250 waveguide depths. Although we did not map out the radial extent of the focus, a simulation using the measured environment which has successfully described this process indicates that the radial size of the focus was on the order of 800 m at a 30 km range and 300 m at a 5 km range.

3.3.2 Stability Measurements

Here we just show examples of stability measurements from the first experiment. Two stability data collection periods for the probe source depths of 40 m and 75 m were made for one hour and two hours, respectively (the lengths of the runs were dictated by experimental circumstance). Figure 22 shows the results of these runs. These plots indicate that the focus was considerably more stable for the deep probe source vs the shallower probe source and that the focus is broader for the shallower probe source. This is consistent with the measured sound speed structure. A discussion on the stability of the TRM will be given in Sec. 5.

3.3.3 TRM with variable range focusing

Here we present results which experimentally confirm a technique to change the range focus of a TRM as described in Sec. 3.3.3 [20]. During the experiment, the frequency shift was implemented in near real-time by a simple FFT bin shift of the probe source data received by the SRA prior to retransmission. Fig. 23(a) shows the considerable defocusing for the PS at a depth of 68 m when the VRA was 600-m inbound of the probe source. Fig. 23(b)-(d) show frequency shifts of 20 Hz, 25 Hz and 32 Hz with the best focus resulting from the 32 Hz shift. It is interesting to note that this latter result corresponds to $\beta = 1.4$, and in essence, this procedure is a way of determining β.

To summarize, it is possible to shift the focal range on the order of 10% of the nominal range of the probe source. The theory on which this shift is dependent is valid only over a frequency range
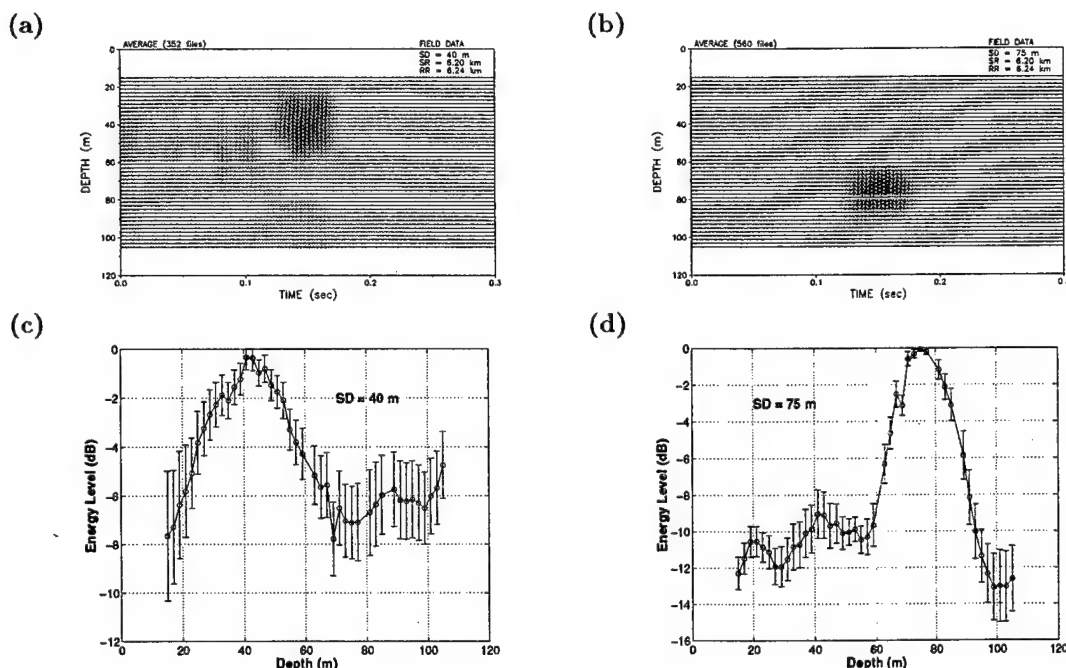
(a)

(b)

(c)

(d)

Figure 22: Results on stability of the focal region. (a) Pulse arrival structure at VRA for probe source at 40-m depth averaged over 1 h. (b) Pulse arrival structure at VRA for probe source at 75-m depth averaged over 2 h. (c) Mean and standard deviation of energy in a 0.3-s window for 40-m probe source. (d) Mean and standard deviation of energy in a 0.3-s window for 75-m probe source.

in which the mode shapes do not change significantly. Frequency shifts of greater than about 10% violate this condition. A practical limitation also comes from the transducer characteristics of the SRA whose resonance around 445 Hz with a 3 dB bandwidth of approximately 35 Hz as shown in Fig. B1 in Ref.[19]. Therefore, it is difficult to excite the pulse at a carrier frequency more than 10% offset from the original resonance frequency.

3.4 Summary of TRM experiments

The description above has been limited mostly to the implementation of a time reversal mirror in the ocean. The experiments also studied other aspects of the TRM process such as stability, fluctuations, range dependence, out of plane defocusing. These topics will be discussed elsewhere in this workshop.

4 The range-dependent ocean waveguide

The factors that control phase-conjugate focusing in severely range-dependent environments will be examined by considering a general non-uniform, non-adiabatic waveguide. The conditions for "ideal" phase-conjugate focusing in such a waveguide will be derived and this will implicitly identify the factors that degrade focusing. To simplify the discussion, only vertical source-receiver arrays will be considered. The main objective is to generalize Eq. 35 to the range-dependent case, using the approach given by
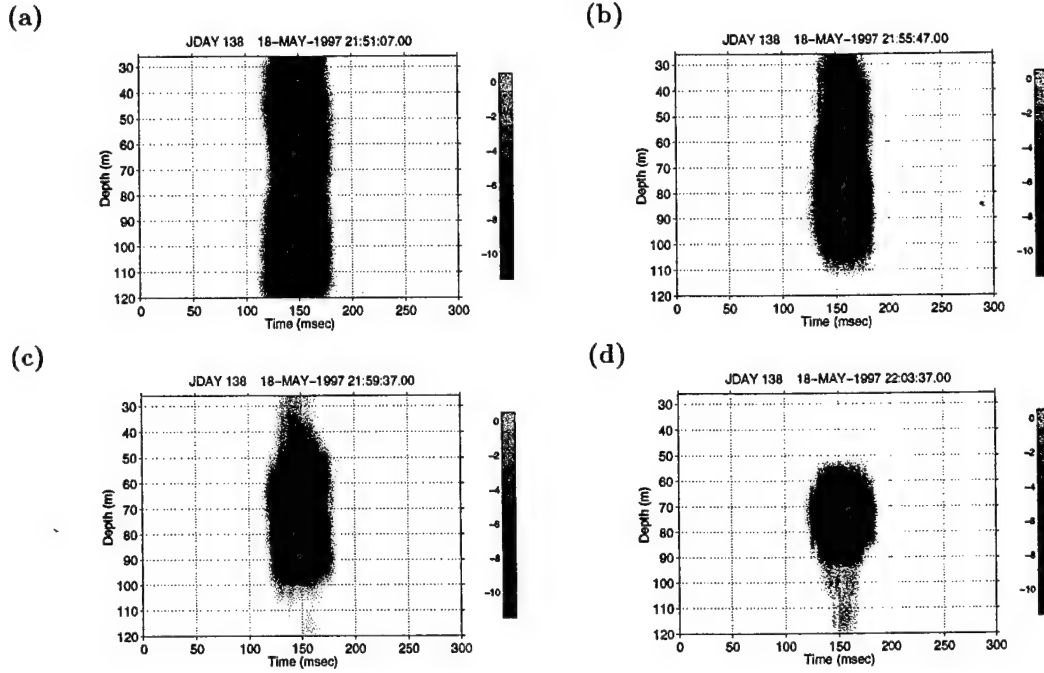
(a)

(b)

(c)

(d)

Figure 23: Experimental results for the PS at a depth of 68 m. (a) Out-of-focus results on the VRA when the VRA is 600 m inbound of the PS. (b) -20 Hz frequency shift. (c) -25 Hz frequency shift. (d) -32 Hz frequency shift. The -32 Hz shift in (d) shows the best focus, which corresponds to $\beta = 1.4$.

Siderius, et al. [32] in connection with the "guide source" concept. In this approach, small regions near the probe source and SRA are assumed to be range-independent, but the larger region between is allowed to have arbitrary range dependence in bathymetry and sound speed. Losses are neglected and will be discussed later in qualitative terms.

The Green's function for the probe field near the probe source is approximated using range-independent normal modes.

$$G_\omega(r, z; R, z_{ps}) = \sum_n \frac{a_n(z_{ps})u_n(R, z)}{\sqrt{k_n(R)|r - R|}} e^{ik_n(R)|r-R|} \quad , \tag{41}$$

Similarly, the Green's function for the probe field at the SRA is written in the form

$$G_\omega(0, z_j; R, z_{ps}) = \sum_n \frac{b_n(z_{ps})u_n(0, z_j)}{\sqrt{k_n(0)R}} e^{ik_n(0)R} \quad . \tag{42}$$

The modal eigenfunctions in the vicinity of the probe source and SRA are denoted $u_n(R, z)$ and $u_n(0, z)$, respectively. The corresponding eigenvalues are $k_n(R)$ and $k_n(0)$. These Green's functions do not bear the superscripts 1 and 2 introduced earlier because a time-invariant environment is under consideration. The subscript ω is used here in the same sense as in the main text. The mode amplitudes for the near-source Green's function are

$$a_n(z_{ps}) = \frac{ie^{-i\pi/4}}{\sqrt{8\pi}\rho(z_{ps})} u_n(R, z_{ps}) \quad , \tag{43}$$
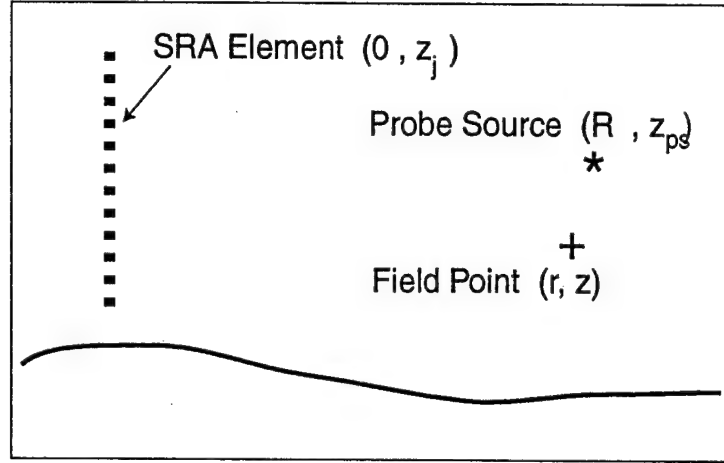
Figure 24: Coordinate definitions for source-receiver array (SRA), probe source, and field point in range-dependent ocean.

and the mode amplitudes for the Green's function near the SRA are given by the linear transformation

$$b_m(z) = \sum_n U_{mn} a_n(z) \quad . \tag{44}$$

For convenience, it is assumed that there are the same number of modes near the source and near the SRA, so that U_{mn} is a square matrix. Cases for which these numbers are similar but not equal can be treated by discarding high-order modes. The matrix U_{mn} includes any mode coupling that is due to the range dependence of the ocean and is defined in such a way as to be independent of source depth. Furthermore, to the extent that absorption loss in the water column and seafloor can be neglected, U_{mn} is unitary:

The field produced by the SRA is

$$P_{pc}(r, z; \omega) = \sum_{j=1}^{J} G_\omega(r, z; 0, z_j) G_\omega^*(0, z_j; R, z_{ps}) \quad . \tag{45}$$

The Green's function for propagation from the jth array element to the field point (r, z) can be expressed in terms of the Green's function for propagation in the opposite direction by using reciprocity:

$$G_\omega(r, z; 0, z_j) = \frac{\rho(z)}{\rho(z_j)} G_\omega(0, z_j; r, z) \quad . \tag{46}$$

In terms of mode amplitudes,

$$G_\omega(r, z; 0, z_j) = \frac{\rho(z)}{\rho(z_j)} \sum_n \frac{c_n(z) u_n(0, z_j)}{\sqrt{k_n(0)r}} e^{ik_n(0)R} \quad , \tag{47}$$

where the mode amplitudes, $c_n(z)$, are

$$c_m(z) = \sum_{n'} U_{mn} a_n(z) e^{ik_n(R)(r-R)} \quad . \tag{48}$$

the mode amplitudes, $c_n(z)$, are essentially the same as the $b_n(z)$, but with the source range
shifted by $r - R$.

ions 42 and 47 can be inserted in Eq. 45 to obtain an expression for the phase-conjugate field
-dependent waveguide.

$$P_{pc}(r, z; \omega) = \frac{\rho(z)}{\sqrt{Rr}} \sum_{m,n} \frac{c_m(z)\Delta_{mn}b_n^*(z_{ps})}{\sqrt{k_m(0)k_n(0)}} \quad , \tag{49}$$

$$\Delta_{mn} = \sum_{j=1}^{J} \frac{u_m(0, z_j)u_n(0, z_j)}{\rho(z_j)} \quad , \tag{50}$$

al case, the SRA spans the entire water column with elements having uniform spacing, d_a,
iodal eigenfunctions have negligible amplitude in the bottom. In this case, the sum over array
in Eq. 50 approximates the orthonormality integral for modal eigenfunctions (Eq. 17), and
in be taken equal to δ_{mn}. This ideal can be approached quite closely in the environment of the
nean experiments. Using the environmental parameters defined in Fig. 17, and considering
irst 12 modes, an array with 36 elements with spacing $d_a = 3.33$ m and with the shallowest
44 m below the surface gives diagonal elements in $\Delta_{mn} d_a$ that are within 3 percent of unity
agonal elements that are of order 0.03 or less.
iing to the derivation of the conditions for ideal phase-conjugate focusing, take $\Delta_{mn} = \delta_{mn}/d_a$
to obtain

$$P_{pc}(r, z; \omega) = \frac{\rho(z)}{d_a\sqrt{Rr}} \sum_{m,n} Q_{mn}a_m(z)a_n^*(z_{ps})e^{ik_n(R)(r-R)} \quad , \tag{51}$$

$$Q_{mn} = \sum_l \frac{U_{lm}U_{ln}^*}{k_l(0)} \quad . \tag{52}$$

due to absorption and scattering are detrimental to phase-conjugate focusing, as they cause
on of higher-order modes, yielding a blurrier focus than would be possible with lower loss.
ore, this blurring will increase as the range between the source and the array increases owing
ong range- and mode-number dependence of attenuation. Figure 25 shows the loss of focus
in a high-loss silty environment as compared to a lower-loss sandy environment. As explained
1.2, losses in the ocean waveguide are primarily due to refraction of energy into the seafloor,
ifloors with relatively high sound speed (sand) are less lossy than seafloors with relatively low
ed (silt). As a result, the sandy environment supports a greater number of acoustic modes,
a sharper focus.
loping the ideal phase conjugation case, losses are set to zero and the mode coupling matrix,
ken to be unitary. If the mode dependence of $k_l(0)$ in Eq. 52 is neglected,

$$Q_{mn} = \frac{\delta_{mn}}{k_m(0)} \quad . \tag{53}$$

hase-conjugate field for an ideal array in a lossless environment can be approximated as

$$P_{pc}(r, z; \omega) = \sum_m \frac{u_m(R, z)u_m(R, z_{ps})e^{ik_m(R)(r-R)}}{8\pi\rho(z_{ps})k_m(0)d_a\sqrt{Rr}} \quad , \tag{54}$$
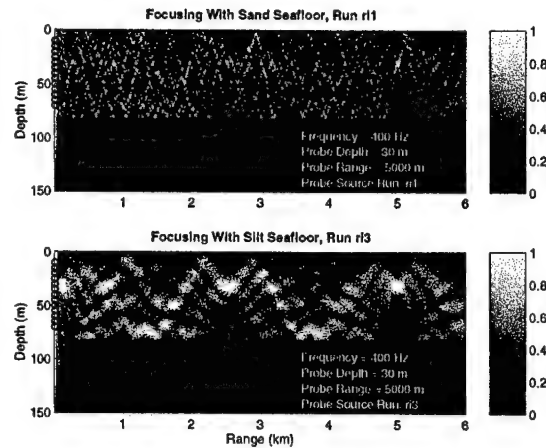
Figure 25: Comparison of focusing for sand and silt seafloors. The sand seafloor has sediment/water density ratio 2.0 and sound speed ratio 1.13, with absorption of 0.135 dB / wavelength. The corresponding numbers for the silt seafloor are 1.5, 1.027 and 0.1. The gray scale is linear in the relative field magnitude.

Apart from inessential factors, this expression is the same as Eq. 35 which was derived for the range-independent case. Even though Eq. 54 represents the ideal case, it illustrates properties that actual phase-conjugate arrays may possess, provided they are not too far from ideal. One such property is independence of the focus pattern upon the distance between the probe source and the array (when absorption can be neglected and apart from the cylindrical spreading factor $1/\sqrt{Rr}$). Even more strikingly, the focus field is independent of the (possibly range-dependent) environment between the focus and the array (see examples presented by Siderius et al. [32]). That is, the focus depends only on the local properties of the water column and sea floor and is not affected by bathymetry or range-dependent water-column properties in the region between the array and the focus, provided the latter do not change appreciably during the two propagation cycles. This means that, in the ideal case, phase conjugation is not affected by time-invariant forward scattering due to bathymetry, fronts, etc. It also implies that, in simulations of phase-conjugate focusing, it is important to accurately model the ocean in the vicinity of the focus, but less accuracy is required for the more distant parts of the propagation path. One important reservation must be added at this point. The derivation above is essentially two-dimensional in that cross-range spatial variation of the ocean is neglected.

Figure 26 shows the results of a simulation which illustrates the invariance of the focus. In this figure, range-dependent and range-independent environments having the same seafloor type (sand) yield very similar focal fields, even though the bathymetry between the probe source and SRA is greatly different in the two cases. This is a non-ideal case with realistic parameters, including loss. Figure 27 shows a case in which losses destroy focus invariance. In this case, the probe source field propagates upslope to reach the SRA. Modes are lost during upslope propagation, leading to a broader focus than in the range-independent situation. In contrast, modes are not lost in the downslope propagation of Fig. 26.

The invariance seen in the ideal ocean waveguide case is similar to that predicted for the ideal, closed array, except that the time-reversed field is a standing wave in the latter case. In the present case, the
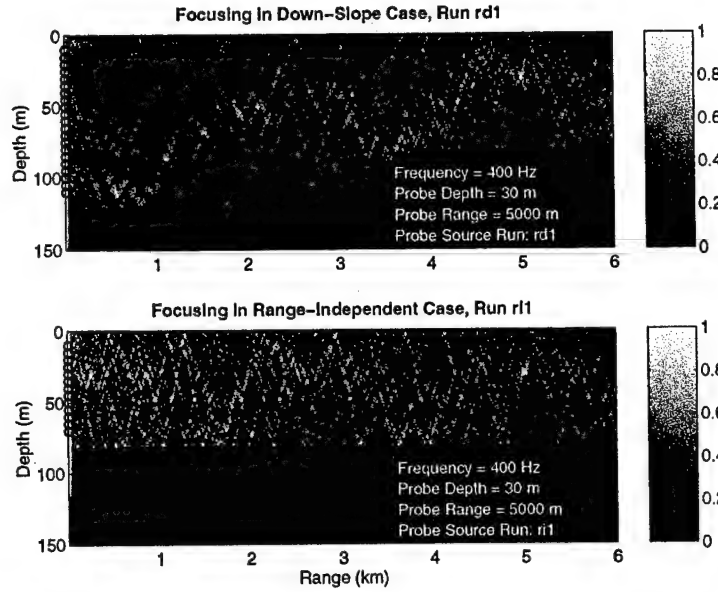
Figure 26: Comparison of focusing for range-independent and range-dependent (downslope propagation of probe source) environments. The sediment acoustic properties are the same as those of the sand seafloor of Fig. 25. The gray scale is linear in the relative field magnitude.

probe source field (including only propagating modes) is given by Eq. 41 which can be put in the form

$$G(r, z; R, z_{ps}) = \frac{ie^{-i\pi/4}}{\rho(z_{ps})\sqrt{8\pi|r - R|}} \sum_n \frac{u_n(R, z)u_n(R, z_{ps})e^{ik_n(R)|r - R|}}{\sqrt{k_n(R)}} \quad . \tag{55}$$

Apart from a difference in spreading loss and an overall phase difference, Eqs. 54 and 55 are quite similar. There is a slight term-by-term difference owing to differing factors involving modal eigenvalues, but the primary difference is in the propagation phase factor. The source field propagates *away* from the source location while the phase conjugate field propagates *past* the source location in the direction away from the SRA.

5   The Effect of Ocean Fluctuations on Phase Conjugation

The ocean is random in several respects. The surface and bottom boundaries are randomly rough, and the seawater is inhomogeneous owing to stratification, turbulence, and internal waves. In addition, wave-generated bubbles introduce inhomogeneity in a layer near the surface, and biological, hydrodynamic, and geophysical processes make the ocean sediment inhomogeneous. Sound scattering due to randomness of the seafloor is time independent, and is not expected to have deleterious effects on phase-conjugate focusing. In fact, the range-independent environment discussed earlier can be considered a kind of scattering example, and it was seen that phase conjugation adapts nicely to the complexities of this case. Generally, phase conjugation can be expected to operate robustly in the presence of time-independent scattering. Problems arise when the scattering is time-dependent, since the medium
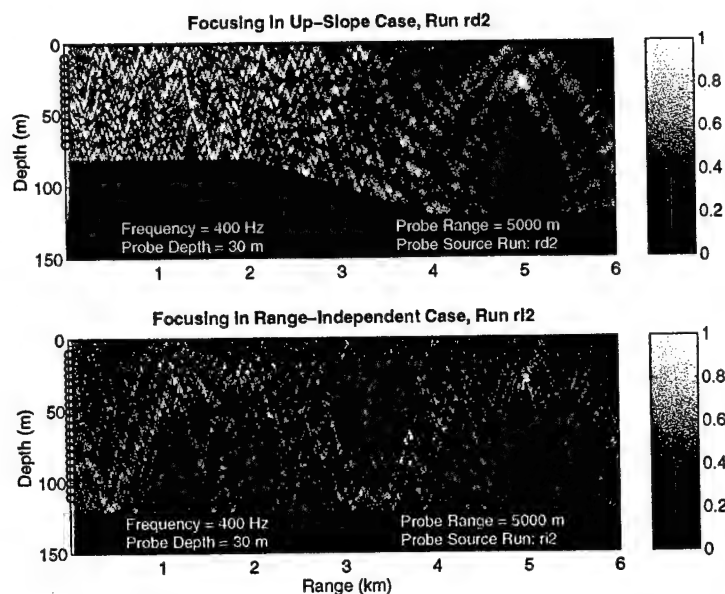
Figure 27: Comparison of focusing for range-independent and range-dependent (upslope propagation of probe source) environments. The sediment acoustic properties and gray scale are the same as those of Fig. 25.

changes between the probe and retransmission cycles. This is the case with scattering by surface waves and internal waves, for which one would like to know the characteristic stability time over which a given probe will yield satisfactory focusing.

5.1 Time-independent volume scattering

As noted above, volume inhomogeneities in the ocean are inherently time dependent, owing to the presence of internal waves. These waves have rather long periods (minutes to hours), however, so that volume scattering can be approximated as time independent if the time between probing and retransmission is sufficiently short. In this case one does not expect scattering to degrade the focus, in fact, it will be seen that the focus is improved by scattering. In static environments, the subscripts 1 and 2 can be dropped in Eq. 12 because there is no change in the environment between the probe transmission and the time-reversed retransmission. It is useful to consider the formal average of the focus field, imagining an ensemble of time-reversal measurements made using a hypothetical ensemble of random environments. Often in underwater acoustics, the average of a field over an ensemble of realizations is not comparable in magnitude to the field seen in single realizations, because scattering often causes fluctuations that are comparable to or greater than the mean. This is not the situation with phase conjugation if the SRA spans an appreciable portion of the water column, as the arguments made in connection with Eq. 55 show that the focus field is not very strongly dependent on perturbations of the environment. Thus, it is useful to examine the average focus field, taking it as an approximation to the field seen in any given realization.
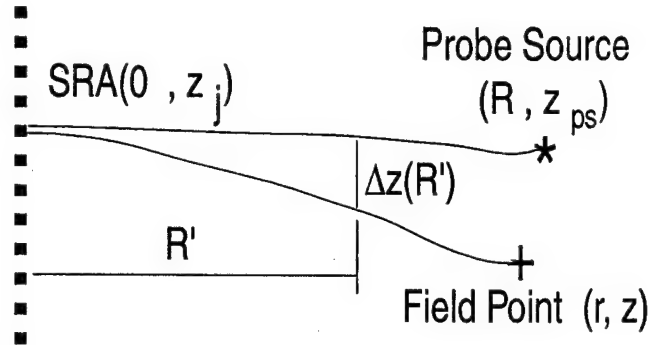
Figure 28: Coordinate definitions for static volume scattering environment.

$$< P_{pc}(\mathbf{r};\omega) >= \sum_{j=1}^{J} K(\mathbf{r}, \mathbf{r}_{ps}, \mathbf{r}_j) \quad , \tag{56}$$

where

$$K(\mathbf{r}, \mathbf{r}_{ps}, \mathbf{r}_j) =< G_\omega(\mathbf{r}, \mathbf{r}_j) G_\omega^*(\mathbf{r}_{ps}, \mathbf{r}_j) > \quad . \tag{57}$$

The first moment of the focus field depends on the second moment of the Green's function. In some simple cases, the second moment of the Green's function is of the form (see [33] for an example and references, and [34] for dynamic case)

$$< G_\omega(r, z, 0, z_j) G_\omega^*(R, z_{ps}, 0, z_j) >= G_{0,\omega}(r, z, 0, z_j) G_{0,\omega}^*(R, z_{ps}, 0, z_j) e^{-H} \tag{58}$$

where

$$H = \frac{\Phi^2}{R_s} \int_0^{R_s} \{1 - \rho[\Delta z(R')]\} dR' \quad , \tag{59}$$

and where $G_{0,\omega}(r, z, 0, z_j)$ is the Green's function for the average medium, $\rho(z)$ is the vertical correlation function for refractive index $(\rho(0) = 1)$, Φ^2 is the phase variance for a path of length R, and $\Delta z(R')$ is vertical separation of ray paths (Fig. 5.1).

Using this result, the mean phase-conjugate field is

$$< P_{pc}(R, z;\omega) >= P_{pc0}(R, z;\omega) e^{-H} \tag{60}$$

where

$$P_{pc0}(R, z;\omega) = \sum_{j=1}^{J} G_{0,\omega}(r, z, 0, z_j) G_{0,\omega}^*(R, z_{ps}, 0, z_j) \tag{61}$$

is the phase-conjugate field for the average medium. Following Uscinski and Reeve [35], expand the correlation function for refractive index fluctuations in a power series:

$$\rho(z) = 1 - \frac{z^2}{l_v^2} + \dots \tag{62}$$

Assuming that the average medium is infinite and non-refractive, the ray paths are straight lines and the integral for H can be performed.

$$H = \frac{\Phi^2(z - z_s)^2}{3 l_v^2} \tag{63}$$

The factor e^{-H} has a Gaussian shape in z centered on the probe source with $1/e$ full width

$$W_v = \frac{2\sqrt{3} l_v}{\Phi} \tag{64}$$

In some cases, this width can be less than the focal spot width for the average medium [14], [36]. This sharpening of the focus has been observed experimentally but in a stronger scattering regime than the present formalism can describe [37].

5.2 Time-dependent scattering by surface waves

Time-dependent forward scattering due to surface waves causes degradation of phase-conjugate focusing. Following Ref. [19], the Green's function will be decomposed into coherent (unscattered) and incoherent (scattered) parts:

$$G_\alpha(\mathbf{r}, \mathbf{r}') = \overline{G}(\mathbf{r}, \mathbf{r}') + \delta G_\alpha(\mathbf{r}, \mathbf{r}') \quad . \tag{65}$$

The subscript α takes on the values 1 and 2 for the probe and conjugate transmission cycles, respectively. The coherent, or mean, Green's function, $\overline{G}(\mathbf{r}, \mathbf{r}')$ is not assigned a subscript because the random time variations are assumed to be stationary in the statistical sense. It will be assumed that sufficient time has elapsed between the probe and conjugate transmission cycles that variations in the two Green's functions are uncorrelated.

$$< \delta G_2(\mathbf{r}_d, \mathbf{r}_c) \delta G_1^*(\mathbf{r}_b, \mathbf{r}_a) > \ = \ < \delta G_2(\mathbf{r}_d, \mathbf{r}_c) \delta G_1(\mathbf{r}_b, \mathbf{r}_a) > \ = \ 0 \quad . \tag{66}$$

This condition was very likely satisfied in the Mediterranean experiments with respect to scattering by surface waves, which have correlation time scales on the order of seconds, while the time between transmission cycles was measured in minutes and hours.

Combining Eqs. 30, 65, and 66, the mean phase-conjugate field is

$$\overline{P}_{pc}(r, z; \omega) = \sum_{j=1}^{J} \overline{G}(\mathbf{r}, \mathbf{r}_j) \overline{G}^*(\mathbf{r}_j, \mathbf{r}_{ps}) \quad , \tag{67}$$

and the variance of the field is

$$\overline{|P_{pc}(r, z; \omega)|^2} - |\overline{P}_{pc}(r, z; \omega)|^2 = \sum_{j=1}^{J} \sum_{j'=1}^{J} [\overline{G}(\mathbf{r}, \mathbf{r}_j) \overline{G}^*(\mathbf{r}, \mathbf{r}_{j'}) K_{jj'}(\mathbf{r}_{ps}) + \tag{68}$$

$$\overline{G}(\mathbf{r}_{ps}, \mathbf{r}_j) \overline{G}^*(\mathbf{r}_{ps}, \mathbf{r}_{j'}) K_{jj'}(\mathbf{r}) + K_{jj'}(\mathbf{r}) K_{jj'}(\mathbf{r}_{ps})] \quad ,$$
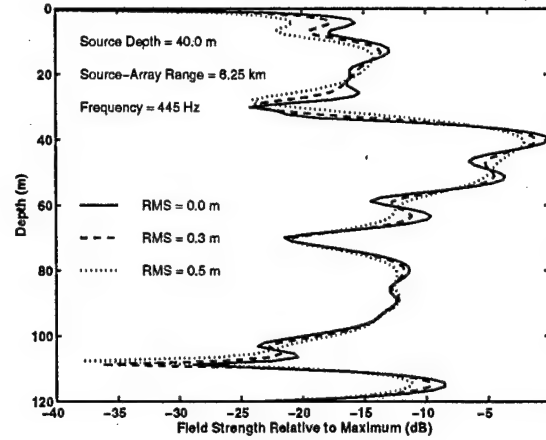
Figure 29: Vertical slice through mean focus for selected RMS surface wave heights.

where

$$K_{jj'}(\mathbf{r}) = <\delta G_\alpha(\mathbf{r}_j, \mathbf{r}) \delta G_\alpha^*(\mathbf{r}_{j'}, \mathbf{r})> \quad . \tag{69}$$

The covariance, $K_{jj'}(\mathbf{r})$, is proportional to the correlation between the incoherent field at elements j and j' of the array, with a unit point source situated at $\mathbf{r}$. In deriving Eq. 68, free use was made of reciprocity (which allows interchange of the two arguments of the Green's function) and stationarity (which means that δG_1 and δG_2 have identical statistics).

Equations 67 and 68 are general and include three-dimensional scattering (i.e., in-plane and out-of-plane scattering). They lead to two general conclusions regarding focusing in ocean experiments for those cases in which sufficient time elapsed between the two transmission cycles. First, the mean focus field, that is, the focus field averaged over many independent probe-conjugate-transmission cycles, is obtained by using the coherent Green's function in place of the actual (random) Green's function. Second, and most important, the field near the focus does not fluctuate appreciably, that is, it is well approximated by the mean focus field. As shown in [19], careful inspection of Eq. 68 shows that the variance of the phase-conjugate field is not localized near the focus, but is spread diffusely in range and depth. Thus, near the focus, the mean field dominates, unless scattering is strong enough to diminish the mean Green's function to such a degree that focusing is essentially destroyed. It is rather straightforward to compute the mean field in the presence of surface-wave scattering [38]. Figure 29 is an example of such a calculation using the modal propagation code, KRAKEN [39] with parameters appropriate to the 1996 Mediterranean experiment. For RMS wave heights within the range measured during the experiment, the degradation of the mean focus is predicted to be slight. This agrees with the experimental fact that the measured focus was stable on the short time scales characteristic of surface wave motion.

5.3   Time-dependent scattering by internal waves

Internal waves are ubiquitous in the ocean and arise because of density stratification. Like surface waves, internal waves involve an interplay of kinetic energy and gravitational potential energy. Internal waves

cause a slow orbital motion of the water which distorts the sound speed profile in both the vertical and horizontal, leading to random inhomogeneity in the acoustic index of refraction. This inhomogeneity, in turn, causes time-dependent fluctuations in sound propagation, which affect the stability of phase conjugation.

In this section, a brief summary of relevant internal wave properties is given, concentrating on the statistical description needed for modeling of propagation fluctuations. For more complete accounts of internal wave dynamics and statistics, see [40] and [41]. For treatments of the problem of acoustic scattering by internal waves, see [42, 43, 44].

The vertical displacement due to internal waves, $\zeta(\mathbf{r}, t)$, can be written as a sum over normal modes

$$\zeta(\mathbf{r}, t) = \sum_{\mathbf{K}} \sum_{j=1}^{J} a_j(\mathbf{K}) W_j(z) e^{i[2\pi f_j(K)t - \mathbf{K} \cdot \mathbf{R}]} \tag{70}$$

where $\mathbf{r} = (\mathbf{R}, z)$, $\mathbf{R} = (x, y)$, $\mathbf{K} = (K_x, K_y)$. The frequencies, $f_j(K)$, and eigenfunctions, $W_j(z)$, are obtained by solving the eigenvalue equation

$$(f_j^2 - f_I^2)W_j'' + K^2[N^2(z) - f_j^2]W_j = 0 \tag{71}$$

subject to the conditions that the displacement field vanishes at the surface ($z = 0$) and bottom ($z = h$). The parameter f_I is the inertial frequency:

$$f_I = 2sin(\theta_L)/T \tag{72}$$

Here, θ_L is the latitude and T is the rotation period of the earth.

The function $N(z)$ is the depth-dependent buoyancy frequency, determined by the vertical gradient of density.

$$N^2(z) = (2\pi)^{-2} \frac{g}{\rho(z)} \frac{\partial}{\partial z}[\rho(z) - \rho_a(z)] \tag{73}$$

where $\rho_a(z)$ is the density profile in an adiabatically mixed ocean, and g is the acceleration of gravity. The eigenfunctions obey the following orthonormality relation:

$$\int_0^h [[N^2(z) - f_I^2]W_j(z)W_{j'}(z)dz = \delta_{jj'} \tag{74}$$

Figure 30 shows a buoyancy frequency profile obtained from oceanographic data in the 1997 Mediterranean experiment [45]. Several of the resulting eigenfunctions, computed for a particular wavenumber are also shown in the figure.

The space-time covariance of the displacement field is defined as the following average,

$$< \zeta(\mathbf{R}_0 + \mathbf{R}, z_1, t + \tau)\zeta(\mathbf{R}_0, z_2, t) >= K(R, z_1, z_2, \tau) \tag{75}$$

where it is assumed that the internal wave field is statistically isotropic and stationary in the transverse directions and stationary with respect to time so that the covariance depends on $R = \sqrt{x^2 + y^2}$ and τ, where (x, y) is the horizontal vector separation of the two points for which the covariance is measured. The displacement field is not stationary in the vertical, hence the covariance depends on both z_1 and z_2. A useful general expression for the covariance can be obtained by squaring and averaging Eq. 70
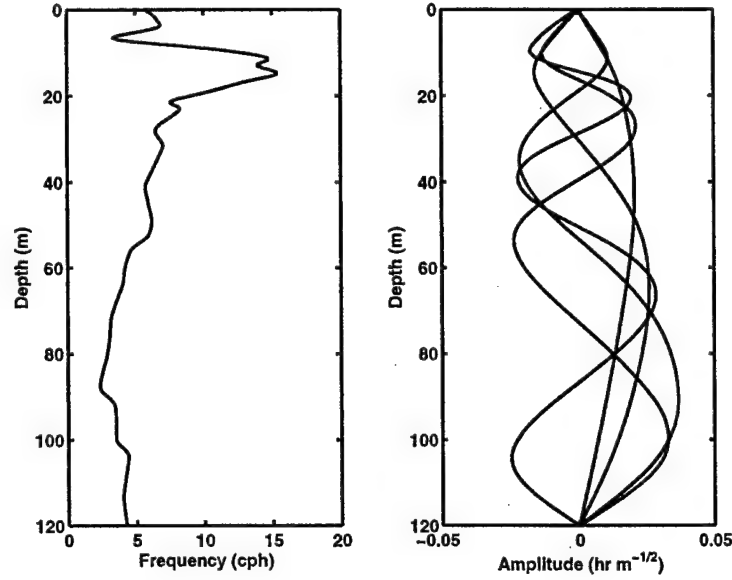
Figure 30: Buoyancy frequency profile and internal wave eigenfunctions for the 1997 Mediterranean experiment. The eigenfunctions are computed for horizontal wavenumber $K = 0.001$ m^{-1}.

$$K(R, z_1, z_2, \tau) = \sum_j \int_{f_I}^{\infty} F(f, j) W_j(z_1) W_j(z_2) J_0(KR) cos(2\pi f\tau) df \qquad (76)$$

The eigenfunctions, $W_j(z)$, and the horizontal wavenumber, K, depend upon both the mode number, j, and the frequency, f.

Henyey et al. [42] provide a shallow-water form of Garrett-Munk internal-wave statistics as follows:

$$F(f, j) = H(j)S(f) \qquad (77)$$

$$H(j) = \frac{n_s}{j^2 + j_*^2} \qquad (78)$$

$$S(f) = \frac{2f_I \sqrt{f^2 - f_I^2} bE_{GM}}{\pi f^3} [\int_0^h N(z) dz]^2 \qquad (79)$$

The two parameters b and E_{GM} appear as a product, and this product (having units of length) is treated as a single parameter determining the energy of the internal wave field. Typically, bE_{GM} is of order 1 m. The parameter n_s is chosen so that the sum of $H(j)$ over all modes is unity. The parameter j_* determines which modes are most important. In deep water, $j_* = 3$ is typical, but smaller values are expected in shallow water [42].

Simulated internal wave displacement fields can be generated by assigning random values to the amplitudes $a_j(\mathbf{K})$ in Eq. 70. The resulting random sound speed field follows from knowledge of the sound speed profile at zero displacement, which may be estimated using an average over several measured profiles. Figure 32 shows simulations of focusing using a probe sent at t = 0. These simulations, for
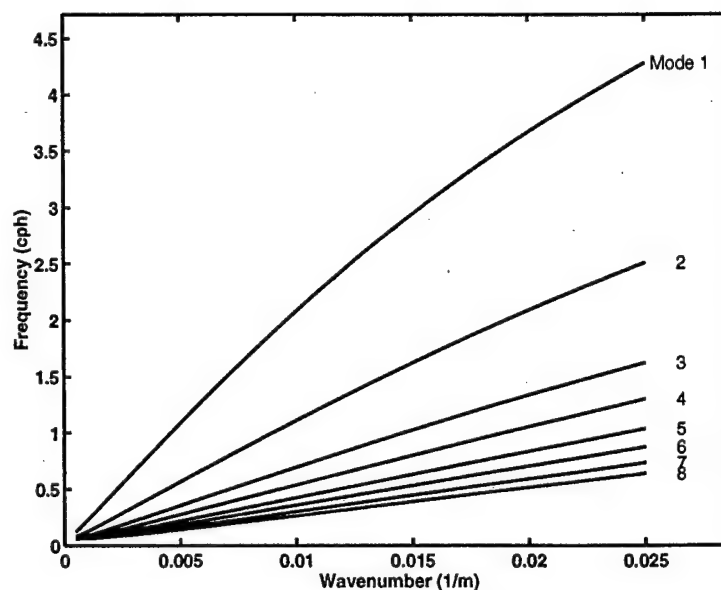
Figure 31: Internal wave frequency vs. wavenumber for the 1997 Mediterranean experiment.

an acoustic frequency of 400 Hz, employed internal wave parameters $j_* = 1$ and $bE_{GM} = 2.0$ m. This value of bE_{GM}, the internal wave energy parameter, is much larger than the value suggested by oceanographic data gathered during the 1997 Mediterranean experiment, $bE_{GM} = 0.135$ m [45]. The smaller, more realistic value produced negligible internal wave effects, consistent with the observed stability of the focus. With the stronger internal wave field, Fig. 32 shows that the initial sharp focus degrades substantially on time scales of several minutes.

6   Conclusions

The ocean is an acoustic waveguide whose fundamental properties are well understood. Prediction of acoustic phenomenon requires extensive ocean acoustic environmental knowledge that is often difficult or impossible to obtain. Matched field processing, a passive localization technique is dependent on accurate acoustic information to construct "replicas" and therefore is extremely sensitive to mismatch. Phase conjugation and time reversal mirrors has been shown to be the active implementation of a matched field processor where an array of sources is used to propagate the measured data on an array back to its origin. In essence, the ocean is used to construct the replica's, eliminating the possibility of mismatch in a reasonably stable ocean environment. Probably the most amazing aspect of implementing a TRM in the ocean over distances as great as 30 km is that the performance of the ocean TRM is almost exactly the same as that of a scaled (MHz regime) ultrasonic TRM implemented in a totally stable laboratory environment out to distances of tens of centimeters [24]. The TRM process is extremely robust.
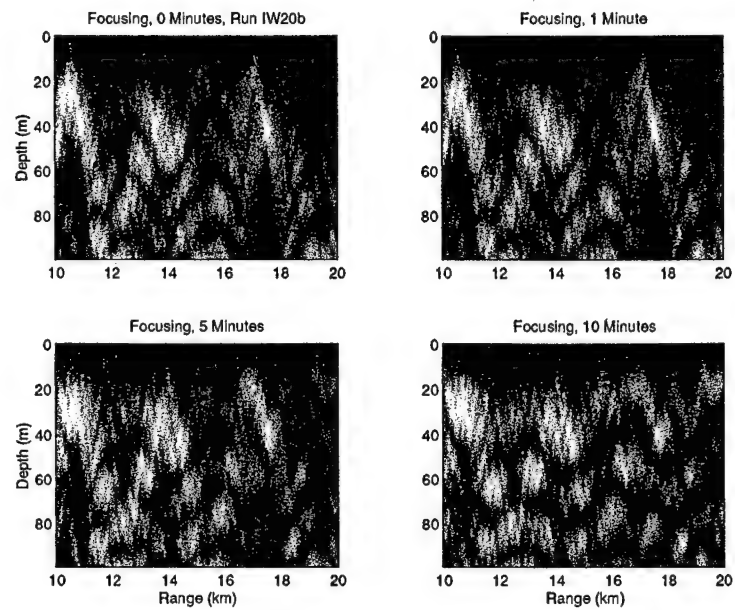
Figure 32: Instability of focus in simulated environment with strong internal wave activity. The gray scale is the same as that of Fig. 25

Acknowledgement

Appendix A: Parabolic Equation Model (PE)

The PE method was introduced into ocean acoustics and made viable with the development of the "split step algorithm" which utilized fast Fourier transforms at each range step [25]. Subsequent numerical developments greatly expanded the applicability of parabolic equation.

Standard PE–Split Step Algorithm

The PE method is presently the most practical and encompassing wave-theoretic range-dependent propagation model. In its simplest form, it is a far-field narrow-angle ($\sim \pm 20°$ with respect to the horizontal—adequate for most underwater propagation problems) approximation to the wave equation. Assuming azimuthal symmetry about a source, we express the solution of Eq. 10 in cylindrical coordinates in a source free region in the form

$$G(r,z) = \psi(r,z) \cdot J(r), \tag{80}$$

and we define $K^2(r,z) \equiv K_0^2 n^2$, n therefore being an "index of refraction" c_0/c, where c_0 is a reference sound speed. Substituting Eq. 80 into Eq. 10 in a source free region and taking K_0^2 as the separation constant , J and ψ satisfy the following two equations:

$$\frac{d^2 J}{dr^2} + \frac{1}{r}\frac{dJ}{dr} + K_0^2 J = 0; \tag{81}$$

$$\frac{\partial^2 \psi}{\partial r^2} + \frac{\partial^2 \psi}{\partial z^2} + \left(\frac{1}{r} + \frac{2}{J}\frac{\partial J}{\partial r}\right) + \frac{\partial \psi}{\partial r} + K_0^2 n^2 \psi - K_0^2 \psi = 0. \tag{82}$$

Equation 81 is a Bessel equation and we take the outgoing solution, a Hankel function, $H_0^1(K_0 r)$, in its asymptotic form and substitute it into Eq. 82, together with the "paraxial" (narrow angle) approximation,

$$\frac{\partial^2 \psi}{\partial r^2} \ll 2K_0 \frac{\partial \psi}{\partial r}, \tag{83}$$

to obtain the parabolic equation (in r),

$$\frac{\partial^2 \psi}{\partial z^2} + 2iK_0 \frac{\partial \psi}{\partial r} + K_0^2 (n^2 - 1)\psi = 0, \tag{84}$$

where we note that n is a function of range and depth. We use a marching solution to solve the parabolic equation. There has been an assortment of numerical solutions but the one that still remains the standard is the so called "split step algorithm" [25].

   We take n to be a constant; the error this introduces can be made arbitrarily small by the appropriate numerical gridding. The Fourier transform of ψ can then be written as

$$\chi(r,s) = \frac{1}{2\pi} \int_{-\infty}^{\infty} \psi(r,z) \exp(-isz)\, dz \tag{85}$$

which together with Eq. 84 gives

$$-s^2 \chi + 2iK_0 \frac{\partial \chi}{\partial r} + K_0^2 (n^2 - 1)\chi = 0. \tag{86}$$

The solution of Eq. 86 is simply

$$\chi(r,s) = \chi(r_0,s) \exp\left[-\frac{K_0^2(n^2-1) - s^2}{2iK_0}(r - r_0)\right], \tag{87}$$

with specified initial condition at r_0. The inverse transform gives the field as a function of depth,

$$\psi(r, z) = \int_{-\infty}^{\infty} \chi(r_0, s) \exp\left[\frac{iK_0}{2}(n^2 - 1)\Delta r\right] \exp\left[-\frac{i\Delta r}{2K_0}s^2\right] \exp(isz) \, ds, \tag{88}$$

where $\Delta r = r - r_0$. Introducing the symbol $\mathcal{F}$ for the Fourier transform operation from the z-domain (as performed in Eq. 85) and $\mathcal{F}^{-1}$ as the inverse transform, Eq. 88 can be summarized by the range-stepping algorithm,

$$\psi(r + \Delta r, z) = \exp\left[\frac{iK_0}{2}(n^2 - 1)\Delta r\right] \mathcal{F}^{-1}\left[\left(\exp(-\frac{i\Delta r}{2K_0}s^2)\right) \cdot \mathcal{F}\left[\psi(r, z)\right]\right], \tag{89}$$

which is often referred to as the "split step" marching solution to the PE. The Fourier transforms are performed using FFT's. Equation 89 is the solution for n constant, but the error introduced when n (profile or bathymetry) varies with range and depth can be made arbitrarily small by increasing the transform size and decreasing the range-step size. It is possible to modify split step algorithm to increase its accuracy with respect to higher angle propagation [26].

Generalized or Higher Order PE Methods

Methods of solving the parabolic equation, including extensions to higher angle propagation, elastic media, and direct time domain solutions including nonlinear effects have recently appeared (see Refs. [27, 28] for additional references). In particular, accurate high angle solutions are important when the environment supports acoustic paths that become more vertical such as when the bottom has a very high speed and hence, large critical angle with respect to the horizontal. In addition, for elastic propagation, the compressional and shear waves span a wide angle interval. Finally, Fourier synthesis for pulse modeling requires high accurate in phase and the high angle PE's are more accurate in phase, even at the low angles.

Equation 82 with the second order range derivative which was neglected because of Ineq. 83 can be written in operator notation as

$$[P^2 + 2iK_0P + K_0^2(Q^2 - 1)]\psi = 0, \tag{90}$$

where

$$P \equiv \frac{\partial}{\partial r}, \quad Q \equiv \sqrt{n^2 + \frac{1}{K_0^2}\frac{\partial^2}{\partial z^2}}. \tag{91}$$

Factoring Eq. 90 assuming weak range dependence and retaining only the factor associated with outgoing propagation yields a one way equation

$$P\psi = iK_0(Q - 1)\psi \tag{92}$$

which is a generalization of the parabolic equation beyond the narrow angle approximation associated with Ineq. 83. If we define $Q = \sqrt{1 + q}$ and expand Q in a Taylor series as a function of q, the standard PE method is recovered by $Q \approx 1 + .5q$. The wide angle PE to arbitrary accuracy in angle, phase, etc.can be obtained from a Padé series representation of the Q operator [27],

$$Q \equiv \sqrt{1 + q} = 1 + \sum_{j=1}^{n} \frac{a_{j,n}q}{1 + b_{j,n}q} + \mathcal{O}(q^{2n+1}), \tag{93}$$

where n is the number of terms in the Padé expansion and

$$a_{j,n} = \frac{2}{2n+1} sin^2 \left(\frac{j\pi}{2n+1} \right), \quad b_{j,n} = cos^2 \left(\frac{j\pi}{2n+1} \right). \tag{94}$$

The solution of Eq. 92 using Eq. 49 has been implemented using finite difference techniques for fluid and elastic media [27]. A "split step" Padé algorithm [29] has recently been developed which greatly enhances the numerical efficiency of this method.

Appendix B: Units

The decibel (dB) is the dominant unit in underwater acoustics and denotes a ratio of intensities (not pressures) expressed in terms of a logarithmic (base 10) scale. Two intensities, I_1 and I_2 have a ratio, I_1/I_2 in decibels of $10 \log I_1/I_2$ dB. Absolute intensities can therefore be expressed by using a reference intensity. The presently accepted reference intensity is based on a reference pressure of one micropascal (μPa): the intensity of a plane wave having an *rms* pressure equal to 10^{-5} dynes per square centimeter. Therefore, taking 1 μPa as I_2, a sound wave having an intensity, of, say, one million times that of a plane wave of *rms* pressure 1 μPa has a level of $10 \log(10^6/1) \equiv 60$ dB re 1 μPa. Pressure (p) ratios are expressed in dB re 1 μPa by taking $20 \log p_1/p_2$ where it is understood that the reference originates from the intensity of a plane wave of pressure equal to 1 μPa.

The average intensity, I, of a plane wave with *rms* pressure p in a medium of density ρ and sound speed c is $I = p^2/\rho c$. In seawater, ρc is 1.5×10^5 g $cm^{-2}s^{-1}$ so that a plane wave of *rms* pressure 1 $dyne/cm^2$ has an intensity of $0.67 \times 10^{-12} W/cm^2$. Substituting the value of a micropascal for the *rms* pressure in the plane wave intensity expression, we find that a plane wave pressure of 1 μPa corresponds to an intensity of $0.67 \times 10^{-22} W/cm^2$ (i.e., 0 dB re 1 μPa).

References

[1] J. Northrup and J. G. Colborn, "Sofar Channel Axial Sound Speed and Depth in the Atlantic Ocean," *J. Geophys. Res.*, 79, p. 5633, (1974).

[2] F. B. Jensen, W. A. Kuperman, M. B. Porter and H. Schmidt, *Computational Ocean Acoustics*, AIP Press, Woodbury, N.Y. (1994).

[3] R. B. Evans, "A coupled mode solution for acoustic propagation in a waveguide with stepwise depth variations of a penetrable bottom," *J. Acoust. Soc. Am*, **74**, p. 188, (1983).

[4] F. B. Jensen and W. A. Kuperman, "Sound propagation in a wedge shaped ocean with a penetrable bottom," *J. Acoust. Soc. Am*, 67, p. 1564, (1980).

[5] A. B. Baggeroer, W. A. Kuperman, and P. N. Mikhalevsky, "An Overview of Matched Field Methods in Ocean Acoustics," *IEEE J. Ocean Eng.* **18**, 401-424 (1993).

[6] H. Schmidt, A.B. Baggeroer, W.A. Kuperman, and E.K. Scheer, "Environmentally tolerant beamforming for high-resolution matched field processing: Deterministic mismatch," *J. Acoust. Soc. Am.* **88**, 1851–1862 (1990).

[7] A.M. Richardson and L.W. Nolte, "*A posteriori* probability source localization in an uncertain sound speed, deep ocean environment," *J. Acoust. Soc. Am.* **89**, 2280–2284 (1991).

[8] J. L. Krolik, "Matched field minimum variance beamforming in a random ocean channel," *J. Acoust. Soc. Am.* **92**, 1408-1419 (1992).

[9] M. D. Collins and W. A. Kuperman, "Focalization: Environmental focusing and source localization," *J. Acoust.Soc. Am.* **90**, 1410-1422 (1991).

[10] B. Y. Zel'dovich, N. F. Pilipetsky and V. V. Shkunov *Principles of Phase Conjugation* (Springer-Verlag, Berlin, 1985)

[11] M. Fink, C. Prada, F. Wu, D. Cassereau, "Self focusing with time reversal mirror in inhomogeneous media," *Proceeding of IEEE Ultrasonics Symposium 1989*, Montreal **2**, 681-686 (1989).

[12] M. Fink, "Time Reversal Mirrors," *Acoustical Imaging* **21**, edited by J. P. Jones, Plenum Press, New York, 1-15 (1995).

[13] D. R. Jackson and D. R. Dowling, "Phase conjugation in underwater acoustics," *J. Acoust. Soc. Am.* **89**, 171-181 (1991).

[14] D. R. Dowling and D. R. Jackson, "Narrow-band performance of phase-conjugate arrays in dynamic random media," *J. Acoust. Soc. Am.* **91**, 3257-3277 (1992).

[15] D. R. Dowling, "Phase-conjugate array focusing in a moving medium," *J. Acoust.Soc. Am.* **94**, 1716-1718 (1993).

[16] D. R. Dowling, "Acoustic pulse compression using passive phase-conjugate processing," *J. Acoust.Soc. Am.* **95**, 1450-1458 (1994).

[17] A. Parvulescu and C. S. Clay, "Reproducibility of signal transmissions in the ocean" *Radio Elec. Eng.* **29**, 223-228 (1965).

[18] A. Parvulescu, "Matched-signal ("Mess") processing by the ocean," *J. Acoust.Soc. Am.* **98**, 943-960 (1995).

[19] W. A. Kuperman, William S. Hodgkiss, Hee Chun Song, T. Akal, C. Ferla and Darell Jackson, "Phase Conjugation in the ocean: Experimental demonstration of an acoustic time-reversal mirror," *J. Acoust. Soc. Am.* **103**, 25-40 (1998).

[20] Hee Chun Song, W. A. Kuperman and W. S. Hodgkiss, "A time-reversal mirror with variable range focusing," *J. Acoust. Soc. Am.* **103**, 3234-3240 (1998).

[21] W. S. Hodgkiss, H. C. Song, W. A. Kuperman, T. Akal, C. Ferla and Darell Jackson, "A long-range and variable focus phase-conjugation experiment in shallow water," *J. Acoust. Soc. Am.* **105**, 1597-1604 (1999).

[22] P. Roux, H.C. Song, M.B. Porter, and W.A. Kuperman, "Application of parabolic equation method to medical ultrasonics," submitted to *Wave Motion* (1999).

[23] R.K. Brienzo and W.S. Hodgkiss, "Broadband matched field processing," *J. Acoust.Soc. Am.* **94**, 2821–2831 (1993).

[24] P.Roux, B. Roman and M.Fink, "Time-reversal in an ultrasonic waveguide," *Appl. Phys. Lett.*, **70**, 1811–1813, (1997).

[25] F. D. Tappert, "The Parabolic Approximation Method," *Wave Propagation and Underwater Acoustics*, (eds.) J. B. Keller and J. S. Papadakis, Springer-Verlag, Berlin, (1977).

[26] D.J. Thomson and N.R. Chapman, "A wide-angle split-step algorithm for the parabolic equation," *J. Acoust. Soc. Am.*, **74**, p. 1848, (1983).

[27] M. D. Collins, "Higher-order Padé approximations for accurate and stable elastic parabolic equations with applications to interface wave propagation," *J. Acoust. Soc. Am.*, **89**, p. 1050, (1991).

[28] B. E. McDonald and W. A. Kuperman, "Time domain formulation for pulse propagation including nonlinear behavior at a caustic," *J. Acoust. Soc. Am*, **81**, p. 1406, (1987).

[29] M. D. Collins "A split-step Padé solution for the parabolic equation method," *J. Acoust. Soc. Am.*, **93**, p. 1736, (1993).

[30] R.P. Porter "Generalized holography as a framework for solving inverse scattering and inverse source problems," *Progrss in Optics XXVII*, (ed.) E. Wolf, Elsevier, New York, (1989).

[31] D. Cassereau and M. Fink, "Focusing with plane time-reversal mirrors: An efficient alternative to closed cavities," J. Acoust. Soc. Am. **94**, 2373-2386 (1992).

[32] M. Siderius, D.R. Jackson, D.Rouseff, and R.P. Porter, "Multipath compensation in range dependent shallow water environments using a virtual receiver", J. Acoust. Soc. Am. **102**, 3439-3449 (1997).

[33] D.R. Jackson and T.E. Ewart, "The effect of internal waves on matched-field processing," J. Acoust. Soc. Am. **96**, 2945-2955 (1994).

[34] S.R. Khosla and D.R. Dowling, "Time-reversing array retrofocusing in simple dynamic underwater environments," J. Acoust. Soc. Am. **104**, 3339-3350 (1998).

[35] B.J. Uscinski and D.E. Reeve, "The effect of ocean inhomogeneities on array output," J. Acoust. Soc. Am. **87**, 2527-2534 (1990).

[36] A.I. Saichev, "Effect of compensating distortions due to scattering in an inhomogeneous medium by use of a reflector turning the front," Radio Eng. Eletron, **27**, 23-30 (1982).

[37] A. Derode, P. Roux, and M. Fink, "Robust time reversal with high-order multiple scattering," Phys. Rev. Lett. **75**, 4206-4209 (1995).

[38] W.A. Kuperman and F. Ingenito, "Attenuation of the coherent component of sound propagating in shallow water with rough boundaries," J. Acoust. Soc. Am. **61**, 1178-1187 (1977),

[39] M.B. Porter, "The KRAKEN normal mode program," SACLANTCEN Memorandum **SM-245**, La Spezia, Italy (1991).

[40] W. Munk, "Internal waves and small-scale processes," *Evolution of Physical Oceanography*, edited by B.A. Warren and C. Wunsch (MIT Press, Cambridge MA, 1981), pp. 264-291.

[41] R. Dashen, W.H. Munk, K.M. Watson, and F. Zachariasen, *Sound Transmission Through a Fluctuating Ocean*, edited by S.M. Flatte (Cambridge University Press, Cambridge, 1979).

[42] F.S. Henyey, D. Rouseff, J.M. Grochocinski, S.A. Reynolds, K.L. Williams, and T.E. Ewart, "Effects of internal waves and turbulence on a horizontal aperture sonar," IEEE J. Oceanic Engr. **22**, 270-280 (1997).

[43] D. Tielbürger, S. Finette, and S. Wolf, "Acoustic propagation through an internal wave field in a shallow water waveguide", J. Acoust. Soc. Am. **101**, 789-808 (1997).

[44] K.B. Winters and E.A. D'Asaro, "Direct simulation of internal wave energy transfer," J. Physical Oceanog. **27**, 1937-1945 (1997).

[45] S.A. Reynolds has analyzed oceanographic data obtained during the 1997 Mediterranean experiment (Private communication).

ONR/MPL REPORT DISTRIBUTION

Office of Naval Research   (3)
Department of the Navy
Ballston Tower One
800 North Quincy Street
Arlington, VA 22217-5660
          Atten: Jeffrey Simmen, ONR 321OA

Regional Director   (1)
ONR Detachment
San Diego Regional Office
4520 Executive Drive, Suite 300
San Diego, CA 92121-3019

Commanding Officer   (1)
Naval Research Laboratory
4555 Overlook Avenue, S.W.
Attn: Code 2627
Washington, D.C. 20375-5320

Defense Technical Information Center   (4)
8725 John J. Kingman Road
Suite 0944
Ft. Belvoir, VA 22060-6218